PHYSICAL REVIEW D **78,** 052005 (2008)

Dalitz plot analysis of the decay $B^0(\bar{B}^0) \to K^{\pm}\pi^{\mp}\pi^0$

B. Aubert,[1] M. Bona,[1] Y. Karyotakis,[1] J. P. Lees,[1] V. Poireau,[1] X. Prudent,[1] V. Tisserand,[1] A. Zghiche,[1] J. Garra Tico,[2] E. Grauges,[2] L. Lopez,[3] A. Palano,[3] M. Pappagallo,[3] G. Eigen,[4] B. Stugu,[4] L. Sun,[4] G. S. Abrams,[5] M. Battaglia,[5] D. N. Brown,[5] J. Button-Shafer,[5] R. N. Cahn,[5] R. G. Jacobsen,[5] J. A. Kadyk,[5] L. T. Kerth,[5] Yu. G. Kolomensky,[5] G. Kukartsev,[5] D. Lopes Pegna,[5] G. Lynch,[5] T. J. Orimoto,[5] I. L. Osipenkov,[5] M. T. Ronan,[5,*] K. Tackmann,[5] T. Tanabe,[5] W. A. Wenzel,[5] P. del Amo Sanchez,[6] C. M. Hawkes,[6] N. Soni,[6] A. T. Watson,[6] H. Koch,[7] T. Schroeder,[7] D. Walker,[8] D. J. Asgeirsson,[9] T. Cuhadar-Donszelmann,[9] B. G. Fulsom,[9] C. Hearty,[9] T. S. Mattison,[9] J. A. McKenna,[9] M. Barrett,[10] A. Khan,[10] M. Saleem,[10] L. Teodorescu,[10] V. E. Blinov,[11] A. D. Bukin,[11] A. R. Buzykaev,[11] V. P. Druzhinin,[11] V. B. Golubev,[11] A. P. Onuchin,[11] S. I. Serednyakov,[11] Yu. I. Skovpen,[11] E. P. Solodov,[11] K. Yu. Todyshev,[11] M. Bondioli,[12] S. Curry,[12] I. Eschrich,[12] D. Kirkby,[12] A. J. Lankford,[12] P. Lund,[12] M. Mandelkern,[12] E. C. Martin,[12] D. P. Stoker,[12] S. Abachi,[13] C. Buchanan,[13] J. W. Gary,[14] F. Liu,[14] O. Long,[14] B. C. Shen,[14,*] G. M. Vitug,[14] L. Zhang,[14] H. P. Paar,[15] S. Rahatlou,[15] V. Sharma,[15] J. W. Berryhill,[16] C. Campagnari,[16] A. Cunha,[16] B. Dahmes,[16] T. M. Hong,[16] D. Kovalskyi,[16] J. D. Richman,[16] T. W. Beck,[17] A. M. Eisner,[17] C. J. Flacco,[17] C. A. Heusch,[17] J. Kroseberg,[17] W. S. Lockman,[17] T. Schalk,[17] B. A. Schumm,[17] A. Seiden,[17] M. G. Wilson,[17] L. O. Winstrom,[17] E. Chen,[18] C. H. Cheng,[18] B. Echenard,[18] F. Fang,[18] D. G. Hitlin,[18] I. Narsky,[18] T. Piatenko,[18] F. C. Porter,[18] R. Andreassen,[19] G. Mancinelli,[19] B. T. Meadows,[19] K. Mishra,[19] M. D. Sokoloff,[19] F. Blanc,[20] P. C. Bloom,[20] W. T. Ford,[20] J. F. Hirschauer,[20] A. Kreisel,[20] M. Nagel,[20] U. Nauenberg,[20] A. Olivas,[20] J. G. Smith,[20] K. A. Ulmer,[20] S. R. Wagner,[20] J. Zhang,[20] R. Ayad,[21,+] A. M. Gabareen,[21] A. Soffer,[21,‡] W. H. Toki,[21] R. J. Wilson,[21] D. D. Altenburg,[22] E. Feltresi,[22] A. Hauke,[22] H. Jasper,[22] J. Merkel,[22] A. Petzold,[22] B. Spaan,[22] K. Wacker,[22] V. Klose,[23] M. J. Kobel,[23] H. M. Lacker,[23] W. F. Mader,[23] R. Nogowski,[23] J. Schubert,[23] K. R. Schubert,[23] R. Schwierz,[23] J. E. Sundermann,[23] A. Volk,[23] D. Bernard,[24] G. R. Bonneaud,[24] E. Latour,[24] V. Lombardo,[24] Ch. Thiebaux,[24] M. Verderi,[24] P. J. Clark,[25] W. Gradl,[25] F. Muheim,[25] S. Playfer,[25] A. I. Robertson,[25] J. E. Watson,[25] Y. Xie,[25] M. Andreotti,[26] D. Bettoni,[26] C. Bozzi,[26] R. Calabrese,[26] A. Cecchi,[26] G. Cibinetto,[26] P. Franchini,[26] E. Luppi,[26] M. Negrini,[26] A. Petrella,[26] L. Piemontese,[26] E. Prencipe,[26] V. Santoro,[26] F. Anulli,[27] R. Baldini-Ferroli,[27] A. Calcaterra,[27] R. de Sangro,[27] G. Finocchiaro,[27] S. Pacetti,[27] P. Patteri,[27] I. M. Peruzzi,[27,§] M. Piccolo,[27] M. Rama,[27] A. Zallo,[27] A. Buzzo,[28] R. Contri,[28] M. Lo Vetere,[28] M. M. Macri,[28] M. R. Monge,[28] S. Passaggio,[28] C. Patrignani,[28] E. Robutti,[28] A. Santroni,[28] S. Tosi,[28] K. S. Chaisanguanthum,[29] M. Morii,[29] J. Wu,[29] R. S. Dubitzky,[30] J. Marks,[30] S. Schenk,[30] U. Uwer,[30] D. J. Bard,[31] P. D. Dauncey,[31] J. A. Nash,[31] W. Panduro Vazquez,[31] M. Tibbetts,[31] P. K. Behera,[32] X. Chai,[32] M. J. Charles,[32] U. Mallik,[32] J. Cochran,[33] H. B. Crawley,[33] L. Dong,[33] V. Eyges,[33] W. T. Meyer,[33] S. Prell,[33] E. I. Rosenberg,[33] A. E. Rubin,[33] Y. Y. Gao,[34] A. V. Gritsan,[34] Z. J. Guo,[34] C. K. Lae,[34] A. G. Denig,[35] M. Fritsch,[35] G. Schott,[35] N. Arnaud,[36] J. Béquilleux,[36] A. D'Orazio,[36] M. Davier,[36] G. Grosdidier,[36] A. Höcker,[36] V. Lepeltier,[36,*] F. Le Diberder,[36] A. M. Lutz,[36] S. Pruvot,[36] P. Roudeau,[36] M. H. Schune,[36] J. Serrano,[36] V. Sordini,[36] A. Stocchi,[36] W. F. Wang,[36] G. Wormser,[36] D. J. Lange,[37] D. M. Wright,[37] I. Bingham,[38] J. P. Burke,[38] C. A. Chavez,[38] J. R. Fry,[38] E. Gabathuler,[38] R. Gamet,[38] D. E. Hutchcroft,[38] D. J. Payne,[38] K. C. Schofield,[38] C. Touramanis,[38] A. J. Bevan,[39] K. A. George,[39] F. Di Lodovico,[39] R. Sacco,[39] G. Cowan,[40] H. U. Flaecher,[40] D. A. Hopkins,[40] S. Paramesvaran,[40] F. Salvatore,[40] A. C. Wren,[40] D. N. Brown,[41] C. L. Davis,[41] N. R. Barlow,[42] R. J. Barlow,[42] Y. M. Chia,[42] C. L. Edgar,[42] G. D. Lafferty,[42] T. J. West,[42] J. I. Yi,[42] J. Anderson,[43] C. Chen,[43] A. Jawahery,[43] D. A. Roberts,[43] G. Simi,[43] J. M. Tuggle,[43] C. Dallapiccola,[44] S. S. Hertzbach,[44] X. Li,[44] T. B. Moore,[44] E. Salvati,[44] S. Saremi,[44] R. Cowan,[45] D. Dujmic,[45] P. H. Fisher,[45] K. Koeneke,[45] G. Sciolla,[45] M. Spitznagel,[45] F. Taylor,[45] R. K. Yamamoto,[45] M. Zhao,[45] S. E. Mclachlin,[46,*] P. M. Patel,[46] S. H. Robertson,[46] A. Lazzaro,[47] F. Palombo,[47] J. M. Bauer,[48] L. Cremaldi,[48] V. Eschenburg,[48] R. Godang,[48] R. Kroeger,[48] D. A. Sanders,[48] D. J. Summers,[48] H. W. Zhao,[48] S. Brunet,[49] D. Côté,[49] M. Simard,[49] P. Taras,[49] F. B. Viaud,[49] H. Nicholson,[50] G. De Nardo,[51] F. Fabozzi,[51,‖] L. Lista,[51] D. Monorchio,[51] C. Sciacca,[51] M. A. Baak,[52] G. Raven,[52] H. L. Snoek,[52] C. P. Jessop,[53] K. J. Knoepfel,[53] J. M. LoSecco,[53] G. Benelli,[54] L. A. Corwin,[54] K. Honscheid,[54] H. Kagan,[54] R. Kass,[54] J. P. Morris,[54] A. M. Rahimi,[54] J. J. Regensburger,[54] S. J. Sekula,[54] Q. K. Wong,[54] N. L. Blount,[55] J. Brau,[55] R. Frey,[55] O. Igonkina,[55] J. A. Kolb,[55] M. Lu,[55] R. Rahmat,[55] N. B. Sinev,[55] D. Strom,[55] J. Strube,[55] E. Torrence,[55] N. Gagliardi,[56] A. Gaz,[56] M. Margoni,[56] M. Morandin,[56] A. Pompili,[56] M. Posocco,[56] M. Rotondo,[56] F. Simonetto,[56] R. Stroili,[56] C. Voci,[56] E. Ben-Haim,[57] H. Briand,[57] G. Calderini,[57] J. Chauveau,[57] P. David,[57] L. Del Buono,[57] Ch. de la Vaissière,[57] O. Hamon,[57] Ph. Leruste,[57] J. Malclès,[57] J. Ocariz,[57] A. Perez,[57] J. Prendki,[57] L. Gladney,[58] M. Biasini,[59] R. Covarelli,[59] E. Manoni,[59] C. Angelini,[60] G. Batignani,[60] S. Bettarini,[60] M. Carpinelli,[60,¶] R. Cenci,[60] A. Cervelli,[60] F. Forti,[60] M. A. Giorgi,[60] A. Lusiani,[60] G. Marchiori,[60] M. A. Mazur,[60] M. Morganti,[60] N. Neri,[60] E. Paoloni,[60] G. Rizzo,[60]

J. J. Walsh,[60] J. Biesiada,[61] Y. P. Lau,[61] C. Lu,[61] J. Olsen,[61] A. J. S. Smith,[61] A. V. Telnov,[61] E. Baracchini,[62] F. Bellini,[62] G. Cavoto,[62] D. del Re,[62] E. Di Marco,[62] R. Faccini,[62] F. Ferrarotto,[62] F. Ferroni,[62] M. Gaspero,[62] P. D. Jackson,[62] M. A. Mazzoni,[62] S. Morganti,[62] G. Piredda,[62] F. Polci,[62] F. Renga,[62] C. Voena,[62] M. Ebert,[63] T. Hartmann,[63] H. Schröder,[63] R. Waldi,[63] T. Adye,[64] G. Castelli,[64] B. Franek,[64] E. O. Olaiya,[64] W. Roethel,[64] F. F. Wilson,[64] S. Emery,[65] M. Escalier,[65] A. Gaidot,[65] S. F. Ganzhur,[65] G. Hamel de Monchenault,[65] W. Kozanecki,[65] G. Vasseur,[65] Ch. Yèche,[65] M. Zito,[65] X. R. Chen,[66] H. Liu,[66] W. Park,[66] M. V. Purohit,[66] R. M. White,[66] J. R. Wilson,[66] M. T. Allen,[67] D. Aston,[67] R. Bartoldus,[67] P. Bechtle,[67] R. Claus,[67] J. P. Coleman,[67] M. R. Convery,[67] J. C. Dingfelder,[67] J. Dorfan,[67] G. P. Dubois-Felsmann,[67] W. Dunwoodie,[67] R. C. Field,[67] T. Glanzman,[67] S. J. Gowdy,[67] M. T. Graham,[67] P. Grenier,[67] C. Hast,[67] W. R. Innes,[67] J. Kaminski,[67] M. H. Kelsey,[67] H. Kim,[67] P. Kim,[67] M. L. Kocian,[67] D. W. G. S. Leith,[67] S. Li,[67] S. Luitz,[67] V. Luth,[67] H. L. Lynch,[67] D. B. MacFarlane,[67] H. Marsiske,[67] R. Messner,[67] D. R. Muller,[67] S. Nelson,[67] C. P. O'Grady,[67] I. Ofte,[67] A. Perazzo,[67] M. Perl,[67] T. Pulliam,[67] B. N. Ratcliff,[67] A. Roodman,[67] A. A. Salnikov,[67] R. H. Schindler,[67] J. Schwiening,[67] A. Snyder,[67] D. Su,[67] M. K. Sullivan,[67] K. Suzuki,[67] S. K. Swain,[67] J. M. Thompson,[67] J. Va'vra,[67] A. P. Wagner,[67] M. Weaver,[67] W. J. Wisniewski,[67] M. Wittgen,[67] D. H. Wright,[67] H. W. Wulsin,[67] A. K. Yarritu,[67] K. Yi,[67] C. C. Young,[67] V. Ziegler,[67] P. R. Burchat,[68] A. J. Edwards,[68] S. A. Majewski,[68] T. S. Miyashita,[68] B. A. Petersen,[68] L. Wilden,[68] S. Ahmed,[69] M. S. Alam,[69] R. Bula,[69] J. A. Ernst,[69] B. Pan,[69] M. A. Saeed,[69] S. B. Zain,[69] S. M. Spanier,[70] B. J. Wogsland,[70] R. Eckmann,[71] J. L. Ritchie,[71] A. M. Ruland,[71] C. J. Schilling,[71] R. F. Schwitters,[71] J. M. Izen,[72] X. C. Lou,[72] S. Ye,[72] F. Bianchi,[73] F. Gallo,[73] D. Gamba,[73] M. Pelliccioni,[73] M. Bomben,[74] L. Bosisio,[74] C. Cartaro,[74] F. Cossutti,[74] G. Della Ricca,[74] L. Lanceri,[74] L. Vitale,[74] V. Azzolini,[75] N. Lopez-March,[75] F. Martinez-Vidal,[75] D. A. Milanes,[75] A. Oyanguren,[75] J. Albert,[76] Sw. Banerjee,[76] B. Bhuyan,[76] K. Hamano,[76] R. Kowalewski,[76] I. M. Nugent,[76] J. M. Roney,[76] R. J. Sobie,[76] P. F. Harrison,[77] J. Ilic,[77] T. E. Latham,[77] G. B. Mohanty,[77] H. R. Band,[78] X. Chen,[78] S. Dasu,[78] K. T. Flood,[78] J. J. Hollar,[78] P. E. Kutter,[78] Y. Pan,[78] M. Pierini,[78] R. Prepost,[78] S. L. Wu,[78] Z. Yu,[78,**] and H. Neal[79]

(*BABAR* Collaboration)

[1]*Laboratoire de Physique des Particules, IN2P3/CNRS et Université de Savoie, F-74941 Annecy-Le-Vieux, France*
[2]*Universitat de Barcelona, Facultat de Fisica, Departament ECM, E-08028 Barcelona, Spain*
[3]*Università di Bari, Dipartimento di Fisica and INFN, I-70126 Bari, Italy*
[4]*University of Bergen, Institute of Physics, N-5007 Bergen, Norway*
[5]*Lawrence Berkeley National Laboratory and University of California, Berkeley, California 94720, USA*
[6]*University of Birmingham, Birmingham, B15 2TT, United Kingdom*
[7]*Ruhr Universität Bochum, Institut für Experimentalphysik 1, D-44780 Bochum, Germany*
[8]*University of Bristol, Bristol BS8 1TL, United Kingdom*
[9]*University of British Columbia, Vancouver, British Columbia, Canada V6T 1Z1*
[10]*Brunel University, Uxbridge, Middlesex UB8 3PH, United Kingdom*
[11]*Budker Institute of Nuclear Physics, Novosibirsk 630090, Russia*
[12]*University of California at Irvine, Irvine, California 92697, USA*
[13]*University of California at Los Angeles, Los Angeles, California 90024, USA*
[14]*University of California at Riverside, Riverside, California 92521, USA*
[15]*University of California at San Diego, La Jolla, California 92093, USA*
[16]*University of California at Santa Barbara, Santa Barbara, California 93106, USA*
[17]*University of California at Santa Cruz, Institute for Particle Physics, Santa Cruz, California 95064, USA*
[18]*California Institute of Technology, Pasadena, California 91125, USA*
[19]*University of Cincinnati, Cincinnati, Ohio 45221, USA*
[20]*University of Colorado, Boulder, Colorado 80309, USA*
[21]*Colorado State University, Fort Collins, Colorado 80523, USA*
[22]*Universität Dortmund, Institut für Physik, D-44221 Dortmund, Germany*
[23]*Technische Universität Dresden, Institut für Kern- und Teilchenphysik, D-01062 Dresden, Germany*
[24]*Laboratoire Leprince-Ringuet, CNRS/IN2P3, Ecole Polytechnique, F-91128 Palaiseau, France*
[25]*University of Edinburgh, Edinburgh EH9 3JZ, United Kingdom*
[26]*Università di Ferrara, Dipartimento di Fisica and INFN, I-44100 Ferrara, Italy*
[27]*Laboratori Nazionali di Frascati dell'INFN, I-00044 Frascati, Italy*
[28]*Università di Genova, Dipartimento di Fisica and INFN, I-16146 Genova, Italy*
[29]*Harvard University, Cambridge, Massachusetts 02138, USA*
[30]*Universität Heidelberg, Physikalisches Institut, Philosophenweg 12, D-69120 Heidelberg, Germany*
[31]*Imperial College London, London, SW7 2AZ, United Kingdom*

[32]University of Iowa, Iowa City, Iowa 52242, USA
[33]Iowa State University, Ames, Iowa 50011-3160, USA
[34]Johns Hopkins University, Baltimore, Maryland 21218, USA
[35]Universität Karlsruhe, Institut für Experimentelle Kernphysik, D-76021 Karlsruhe, Germany
[36]Laboratoire de l'Accélérateur Linéaire, IN2P3/CNRS et Université Paris-Sud 11, Centre Scientifique d'Orsay, B. P. 34, F-91898 ORSAY Cedex, France
[37]Lawrence Livermore National Laboratory, Livermore, California 94550, USA
[38]University of Liverpool, Liverpool L69 7ZE, United Kingdom
[39]Queen Mary, University of London, E1 4NS, United Kingdom
[40]University of London, Royal Holloway and Bedford New College, Egham, Surrey TW20 0EX, United Kingdom
[41]University of Louisville, Louisville, Kentucky 40292, USA
[42]University of Manchester, Manchester M13 9PL, United Kingdom
[43]University of Maryland, College Park, Maryland 20742, USA
[44]University of Massachusetts, Amherst, Massachusetts 01003, USA
[45]Massachusetts Institute of Technology, Laboratory for Nuclear Science, Cambridge, Massachusetts 02139, USA
[46]McGill University, Montréal, Québec, Canada H3A 2T8
[47]Università di Milano, Dipartimento di Fisica and INFN, I-20133 Milano, Italy
[48]University of Mississippi, University, Mississippi 38677, USA
[49]Université de Montréal, Physique des Particules, Montréal, Québec, Canada H3C 3J7
[50]Mount Holyoke College, South Hadley, Massachusetts 01075, USA
[51]Università di Napoli Federico II, Dipartimento di Scienze Fisiche and INFN, I-80126, Napoli, Italy
[52]NIKHEF, National Institute for Nuclear Physics and High Energy Physics, NL-1009 DB Amsterdam, The Netherlands
[53]University of Notre Dame, Notre Dame, Indiana 46556, USA
[54]Ohio State University, Columbus, Ohio 43210, USA
[55]University of Oregon, Eugene, Oregon 97403, USA
[56]Università di Padova, Dipartimento di Fisica and INFN, I-35131 Padova, Italy
[57]Laboratoire de Physique Nucléaire et de Hautes Energies, IN2P3/CNRS, Université Pierre et Marie Curie-Paris6, Université Denis Diderot-Paris7, F-75252 Paris, France
[58]University of Pennsylvania, Philadelphia, Pennsylvania 19104, USA
[59]Università di Perugia, Dipartimento di Fisica and INFN, I-06100 Perugia, Italy
[60]Università di Pisa, Dipartimento di Fisica, Scuola Normale Superiore and INFN, I-56127 Pisa, Italy
[61]Princeton University, Princeton, New Jersey 08544, USA
[62]Università di Roma La Sapienza, Dipartimento di Fisica and INFN, I-00185 Roma, Italy
[63]Universität Rostock, D-18051 Rostock, Germany
[64]Rutherford Appleton Laboratory, Chilton, Didcot, Oxon, OX11 0QX, United Kingdom
[65]DSM/Dapnia, CEA/Saclay, F-91191 Gif-sur-Yvette, France
[66]University of South Carolina, Columbia, South Carolina 29208, USA
[67]Stanford Linear Accelerator Center, Stanford, California 94309, USA
[68]Stanford University, Stanford, California 94305-4060, USA
[69]State University of New York, Albany, New York 12222, USA
[70]University of Tennessee, Knoxville, Tennessee 37996, USA
[71]University of Texas at Austin, Austin, Texas 78712, USA
[72]University of Texas at Dallas, Richardson, Texas 75083, USA
[73]Università di Torino, Dipartimento di Fisica Sperimentale and INFN, I-10125 Torino, Italy
[74]Università di Trieste, Dipartimento di Fisica and INFN, I-34127 Trieste, Italy
[75]IFIC, Universitat de Valencia-CSIC, E-46071 Valencia, Spain
[76]University of Victoria, Victoria, British Columbia, Canada V8W 3P6
[77]Department of Physics, University of Warwick, Coventry CV4 7AL, United Kingdom
[78]University of Wisconsin, Madison, Wisconsin 53706, USA
[79]Yale University, New Haven, Connecticut 06511, USA
(Received 28 November 2007; published 12 September 2008)

[*]Deceased.
[+]Now at Temple University, Philadelphia, PA 19122, USA.
[‡]Now at Tel Aviv University, Tel Aviv, 69978, Israel.
[§]Also with Università di Perugia, Dipartimento di Fisica, Perugia, Italy.
[‖]Also with Università della Basilicata, Potenza, Italy.
[¶]Also with Universita' di Sassari, Sassari, Italy.
[**]Now at Cadence Design Systems Inc., San Jose, CA 95134, USA.

We report a Dalitz-plot analysis of the charmless hadronic decays of neutral B mesons to $K^{\pm}\pi^{\mp}\pi^0$. With a sample of $(231.8 \pm 2.6) \times 10^6 Y(4S) \to B\bar{B}$ decays collected by the *BABAR* detector at the PEP-II asymmetric-energy B Factory at SLAC, we measure the magnitudes and phases of the intermediate resonant and nonresonant amplitudes for B^0 and $\bar{B}^0$ decays and determine the corresponding CP-averaged branching fractions and charge asymmetries. The inclusive branching fraction and CP-violating charge asymmetry are measured to be $\mathcal{B}(B^0 \to K^+\pi^-\pi^0) = (35.7^{+2.6}_{-1.5} \pm 2.2) \times 10^{-6}$ and $\mathcal{A}_{CP} = -0.030^{+0.045}_{-0.051} \pm 0.055$ where the first errors are statistical and the second systematic. We observe the decay $B^0 \to K^{*0}(892)\pi^0$ with the branching fraction $\mathcal{B}(B^0 \to K^{*0}(892)\pi^0) = (3.6^{+0.7}_{-0.8} \pm 0.4) \times 10^{-6}$. This measurement differs from zero by 5.6 standard deviations (including the systematic uncertainties). The selected sample also contains $B^0 \to \bar{D}^0\pi^0$ decays where $\bar{D}^0 \to K^+\pi^-$, and we measure $\mathcal{B}(B^0 \to \bar{D}^0\pi^0) = (2.93 \pm 0.17 \pm 0.18) \times 10^{-4}$.

DOI: 10.1103/PhysRevD.78.052005 PACS numbers: 13.66.Bc, 13.25.−k, 13.25.Hw, 13.25.Gv

I. INTRODUCTION

Amplitude analyses of three-body decays of B mesons with no charm particle in the final state are well suited to study the Cabibbo-Kobayashi-Maskawa (CKM) framework [1] for charged current weak interactions. In the analysis of a Dalitz plot the strong phase motions along the line shapes of interfering resonances are measured and can be used to constrain the weak phases related to the CKM parameters which, in the standard model, govern CP violation. Following the path [2–4] of the 3-pion B meson decays which give constraints on the CKM angle $\alpha_{\rm CKM} \equiv \arg(-V_{td}V_{tb}^*/V_{ud}V_{ub}^*)$, it has been shown in [5,6] that B decays into a kaon and two pions are sensitive to the angle $\gamma_{\rm CKM} \equiv \arg(-V_{ud}V_{ub}^*/V_{cd}V_{cb}^*)$.

In this paper we present a time independent amplitude analysis of the flavor-specific $B^0 \to K^+\pi^-\pi^0$ decay [7] which finalizes preliminary studies [8,9]. The analysis compares the Dalitz plots of the B^0 and $\bar{B}^0$ decays where low-mass $K\pi$ and $\pi\pi$ resonances interfere. Previous measurements of the three-body final state [10,11] and subdecays [12,13] to a vector and a pseudoscalar meson have been published. Other $B \to K\pi\pi$ decays have been studied in [14–17]. A phenomenological study of three-body B meson decays without charm in the final state is presented in [18].

This paper is organized as follows. We first present in Sec. II the decay model based on an isobar expansion of the three-body decay amplitude. The complex coefficients of the expansion are the unknowns we seek to determine by means of an unbinned extended maximum likelihood fit. We describe the detector and data set in Sec. III, the procedure used to select the data sample in Sec. IV, and the fit method in Sec. V. The results are then described in Sec. VI followed by the accounting of the systematic uncertainties in Sec. VII. Finally, in Sec. VIII, we summarize our findings and present an interpretation of our results.

II. DECAY AMPLITUDES

The $B^0 \to K^+\pi^-\pi^0$ decay amplitude is a function of two independent kinematic variables commonly chosen to be the invariant masses squared,[1] $x = m^2_{K^{\pm}\pi^{\mp}}$ and $y = m^2_{K^{\pm}\pi^0}$. The Dalitz plot (DP) is the x, y bidimensional distribution. It is customary to express the decay amplitude as a sum over intermediate (isobar) states:

$$\mathcal{A}(x, y) = \sum_j t_j e^{i\phi_j} f_j(x, y), \tag{1}$$

and similarly for the $\bar{B}^0 \to K^-\pi^+\pi^0$ Dalitz plot,

$$\bar{\mathcal{A}}(x, y) = \sum_j \bar{t}_j e^{i\bar{\phi}_j} f_j(x, y). \tag{2}$$

The isobar coefficients $t_j e^{i\phi_j}$ are constant over the Dalitz plot. For each decay channel, the isobar phase ϕ_j is the sum of a strong phase, the same for B^0 and $\bar{B}^0$ decays, and a weak phase which changes sign. The decay dynamics of an intermediate state are described by the $f_j(x, y)$ function which structures the Dalitz plot. For instance, a resonance formed in the $K^+\pi^-$ system gives a contribution which factorizes as

$$f_j(x, y) = R_j(x) \times T_j(x, y) \times WB_j(x), \tag{3}$$

where $R_j(x)$ is the resonance mass distribution or line shape and $T_j(x, y)$ models the angular dependence. $WB_j(x) = \sqrt{B_B(Rp^*(x))B_j(Rq(x))}$, the product of Blatt-Weisskopf damping factors [19], slightly deviates from unity as a function of x through the breakup momenta[2] of the (quasi) two-body B and resonance decays multiplied by a range parameter R. The f_j are normalized,

$$\int_{\rm DP} |f_j(x, y)|^2 dx dy = 1. \tag{4}$$

We use the Zemach tensor formalism [20,21] for the angular distribution $T_j^{(J)}(x, y)$ of a process by which a pseudoscalar B meson produces a spin-J resonance in

[1]We use natural units where $\hbar = c = 1$ in our algebraic equations.

[2]p^*, the momentum of the bachelor particle in the B meson rest frame, is equal to the breakup momentum of the studied B meson decay.

TABLE I. The *nominal model* for the decay $B^0 \to K^+\pi^-\pi^0$ comprises a nonresonant part and five intermediate states. The three types of line shapes are described in the text. The resonance masses and widths are from [22], except for the LASS shape [23]. We use the same LASS parameters for both neutral and charged $K\pi$ systems. *Additional resonances* that may contribute are included in extended models which we study to estimate the systematic uncertainties.

Intermediate state	Line shape	Parameters
Nominal model		
Nonresonant	Constant	
$\rho^-(770)$	GS	
$K^{*+}(892)$	RBW	
$K^{*0}(892)$	RBW	
$(K\pi)_0^{*+}$	LASS	$m^0 = 1415 \pm 3$ MeV/c^2
$(K\pi)_0^{*0}$		$\Gamma^0 = 300 \pm 6$ MeV
		cutoff $m_j^{\max} = 2000$ MeV/c^2
		$a = 2.07 \pm 0.10$ (GeV/c)$^{-1}$
		$r = 3.32 \pm 0.34$ (GeV/c)$^{-1}$
Additional resonances		
$\rho(1450)$	GS	$m = 1439$ MeV/c^2
		$\Gamma^0 = 550$ MeV
$\rho(1700)$	GS	$m = 1795$ MeV/c^2
		$\Gamma^0 = 278$ MeV
$K_2^*(1430)^{+,0}$	RBW	
$K^*(1680)^{+,0}$	RBW	

association with a bachelor pseudoscalar meson. For $J = 0, 1, 2$, we have

$$T_j^{(0)} = 1, \qquad T_j^{(1)} = -2\vec{p}\cdot\vec{q}, \qquad T_j^{(2)} = \tfrac{4}{3}[3(\vec{p}\cdot\vec{q})^2 - (|\vec{p}||\vec{q}|)^2], \tag{5}$$

where[3] $\vec{p}(x, y)$ $[\vec{q}(x)]$ is the momentum vector of the bachelor particle (the resonance decay product Q defined below) measured in the resonance rest frame. For a neutral (charged) $K\pi$ resonance, Q is the pion (kaon), and for a dipion resonance, Q is the π^0. Notice that these choices define for each two-body system the helicity angle $\theta_j = (\vec{p}_j, \vec{q}_j)$ between 0 and π.

Our nominal model (Table I) for the decay $B^0 \to K^+\pi^-\pi^0$ includes a nonresonant contribution (NR) which is uniformly distributed over the Dalitz plot, and five resonant intermediate states: $\rho^-(770)$, $K^*(892)^{+,0}$, and $(K\pi)_0^{*+,0}$. The latter notation introduced by the *BABAR* experiment [14] denotes phenomenological amplitudes describing the neutral and charged $(K\pi)$ S-waves each by a coherent superposition of an elastic effective-range term and a term for the $K_0^*(1430)$ scalar resonance. It describes current knowledge of low energy $K\pi$ systems with a small number of parameters. Variations to the nominal model are used to estimate the model-dependent systematic uncertainty in the results. Three line-shape parametrizations $R_j(x)$ are used. Parameters are taken from [22] unless stated otherwise.

[3]For simplicity, we have dropped the j index in $\vec{p}$ and $\vec{q}$.

A. Line shapes

1. The relativistic Breit-Wigner distribution

The relativistic Breit-Wigner (RBW) parametrization is used for $K^*(892)^{+,0}$, $K_2^*(1430)^{+,0}$, and $K^*(1680)^{+,0}$:

$$R_j^{(J)}(x; m_j, \Gamma_j^0) = \frac{1}{m_j^2 - x - im_j\Gamma_j^{(J)}(x)}. \tag{6}$$

The mass dependence of the total width $\Gamma_j^{(J)}$ can be ignored for high-mass states. For the low-mass states which decay only elastically, it is defined by

$$\Gamma_j^{(J)}(x) = \Gamma_j^0 \frac{m_j}{\sqrt{x}}\left(\frac{q(x)}{q(m_j^2)}\right)^{2J+1} \frac{B^{(J)}(Rq(x))}{B^{(J)}(Rq(m_j^2))}, \tag{7}$$

where m_j is the mass of the resonance j, $\Gamma_j^0 = \Gamma_j(m_j^2)$ is its width, and the barrier factors (squares of the Blatt-Weisskopf damping factors [19]) are

$$B^{(0)} = 1, \qquad B^{(1)} = \frac{1}{1 + R^2q^2}, \qquad B^{(2)} = \frac{1}{9 + 3R^2q^2 + R^4q^4}. \tag{8}$$

All range parameters were set to $R = 0$ in the analysis, but we checked that the systematic deviations associated with more realistic values taken or interpolated from [24] are below the numerical accuracy we use to quote our results.

2. The Gounaris-Sakurai distribution

The Gounaris-Sakurai (GS) parametrization [25] [Eq. (9)] is used for $\rho^-(770)$, $\rho^-(1450)$, and $\rho^-(1700)$:

$$R_j^{\mathrm{GS}}(x; m_j, \Gamma_j^0) = \frac{1 + d_j\Gamma_j^0/m_j}{m_j^2 + f_j(x) - x - im_j\Gamma_j(x)}, \tag{9}$$

with the same x dependence of the width as for the RBW. The expressions of the constant d_j and the function $f_j(x)$ in terms of m_j and Γ_j^0 are given in Ref. [25].

3. The LASS distribution

For the $K\pi$ S-wave resonances, $(K\pi)_0^{*+,0}$, which dominate for $m_{K\pi}$ below $m_j^{\max} = 2$ GeV/c^2, an effective-range parametrization was suggested [26] to describe the slowly increasing phase as a function of the $K\pi$ mass. We use the parametrization as in the LASS experiment [23], tuned for B decays:

$$R_j^{\rm LASS}(x; m_j^0, \Gamma_j^0, a, r) = \frac{\sqrt{x}}{q\cot\delta_B - iq} + e^{2i\delta_B}\frac{m_j^0\Gamma_j^0\frac{m_j^0}{q_0}}{[(m_j^0)^2 - x] - im_j^0\Gamma_j^0\frac{q}{\sqrt{x}}\frac{m_j^0}{q_0}}, \quad (10)$$

where

$$\cot\delta_B = \frac{1}{aq(x)} + \frac{1}{2}rq(x), \quad (11)$$

a is the scattering length, and r is the effective range (Table I). A LASS isobar coherently comprises the actual $K_0^*(1430)$ (82%), the effective-range term (57%), and the (destructive) interference term (39%).

In this analysis we use a maximum likelihood fit to measure the inclusive branching fraction and CP-violation asymmetry,

$$\mathcal{B}^{\rm incl} \equiv \mathcal{B}(B^0 \to K^+\pi^-\pi^0), \quad (12)$$

$$\mathcal{A}_{CP} \equiv \frac{\int_{\rm DP}[|\bar{\mathcal{A}}(x,y)|^2 - |\mathcal{A}(x,y)|^2]dxdy}{\int_{\rm DP}[|\bar{\mathcal{A}}(x,y)|^2 + |\mathcal{A}(x,y)|^2]dxdy}, \quad (13)$$

as well as the isobar fractions FF_j (CP averaged over B^0 and $\bar{B}^0$) and the CP-violation charge asymmetries:

$$FF_k = \frac{\int_{\rm DP}[|t_k e^{i\phi_k} f_k(x,y)|^2 + |\bar{t}_k e^{i\bar{\phi}_k}\bar{f}_k(x,y)|^2]dxdy}{\int_{\rm DP}[|\sum_j t_j e^{i\phi_j} f_j(x,y)|^2 + |\sum_j \bar{t}_j e^{i\bar{\phi}_j}\bar{f}_j(x,y)|^2]dxdy},$$
$$A_{CP}^k = \frac{\bar{t}_k^2 - t_k^2}{\bar{t}_k^2 + t_k^2}, \quad (14)$$

and the isobar phases relative to those of the $K^{*\pm}\pi^{\mp}$ channel. In those expressions, t_j and $\bar{t}_j$ are the fitted magnitudes for the intermediate state j; ϕ_j and $\bar{\phi}_j$ are the fitted relative phases. Note that, due to interference, the fractions FF_k, in general, do not add up to unity. Nevertheless, we define the quasi-two-body branching fraction for an intermediate state j as follows:

$$\mathcal{B}_j \equiv FF_j \cdot \mathcal{B}^{\rm incl}. \quad (15)$$

B. The square Dalitz plot

The accessible phase space of charmless three-body B decays is unusually large. Most contributing resonances have masses much lower than the B mass. Hence, signal events cluster along the Dalitz-plot boundaries. This is also true for background events. Past experience has shown that another set of variables, defining the *square Dalitz plot* (SDP) [27], is well suited to such configurations. It is defined by the mapping

$$dxdy \to dm'd\theta',$$
$$m' \equiv \frac{1}{\pi}\arccos\left(2\frac{m - m_{\rm min}}{m_{\rm max} - m_{\rm min}} - 1\right),$$
$$\theta' \equiv \frac{1}{\pi}\theta, \quad (16)$$

where $m = \sqrt{x}$ and θ are, respectively, the invariant mass and helicity angle of the $K^{\pm}\pi^{\mp}$ system. $m_{\rm max} = m_B - m_{\pi^0}$ and $m_{\rm min} = m_{K^+} + m_{\pi^-}$ are the kinematic limits of m. The new variables both range between 0 and 1.

III. THE *BABAR* DETECTOR AND DATA SET

The data used in this analysis were collected with the *BABAR* detector at the PEP-II asymmetric e^+e^- storage rings between October 1999 and July 2004. The sample integrates a luminosity of 210.6 fb^{-1} taken on the peak of the $\Upsilon(4S)$ resonance (on resonance) corresponding to $N_{B\bar{B}} = (231.8 \pm 2.6) \times 10^6$ $B\bar{B}$ pairs, and 21.6 fb^{-1} recorded at a center-of-mass (CM) energy 40 MeV below (off resonance).

A detailed description of the *BABAR* detector is given in [28]. Charged-particle trajectories are measured by a five-layer, double-sided silicon vertex tracker (SVT) and a 40-layer drift chamber (DCH) immersed in a 1.5 T magnetic field. Charged-particle identification is achieved by combining the information from a ring-imaging Cherenkov device with the ionization energy loss (dE/dx) measurements from the DCH and SVT. Photons are detected in a CsI(Tl) electromagnetic calorimeter (EMC) inside the coil. Muon candidates are identified in the instrumented flux return of the solenoid. We use GEANT4-based [29] software to simulate the detector response and account for the varying beam and environmental conditions.

IV. EVENT SELECTION

A. Signal selection and background rejection

To reconstruct $B^0 \to K^+\pi^-\pi^0$ decays, we select two charged particles and two photons. The charged-particle candidates are required to have transverse momenta above 100 MeV/c and at least 12 hits in the DCH. They must not be identified as electrons, muons, or protons. A K^+ candidate must be identified as a kaon (with a misidentification probability smaller than 4%) and a π^- candidate must not be identified as a kaon (with a misidentification probability smaller than 7%). The misidentification probabilities are momentum dependent and therefore vary across the Dalitz plot. A π^0 candidate is built from a pair of photon candidates, each with an energy greater than 50 MeV in the laboratory frame (LAB) and a lateral energy deposition profile in the EMC consistent with an electromagnetic shower. The invariant mass of a π^0 candidate must satisfy $0.11 < m_{\gamma\gamma} < 0.16$ GeV/c^2, a wide enough window to accommodate the variation of the resolution across the Dalitz plot from 4.5 to 8 MeV/c^2.

At the $\Upsilon(4S)$ resonance, B mesons are characterized by two nearly independent kinematic variables, the beam energy substituted mass and the energy difference:

$$m_{\rm ES} = \sqrt{(s/2 + \vec{p}_0 \cdot \vec{p}_B)^2/E_0^2 - p_B^2}, \quad (17)$$

$$\Delta E = E_B^* - \sqrt{s}/2, \quad (18)$$

where E and p are energy and momentum, and the subscripts 0 and B refer to the e^+e^--beam system and the B candidate, respectively; s is the square of the center-of-mass energy and the asterisk labels the CM frame. We require that $m_{\rm ES} > 5.27$ GeV$/c^2$. To avoid a bias in the Dalitz plot from the dependence on the π^0 energy of the resolution in ΔE, we introduce the dimensionless quantity

$$\Delta E' \equiv \frac{2\Delta E - (\Delta E_{\rm max} + \Delta E_{\rm min})}{\Delta E_{\rm max} - \Delta E_{\rm min}} \quad (19)$$

where the bounds obtained from simulation, $\Delta E_{\rm max} = 0.08 - 0.0014 \cdot m_{K^+\pi^-}$, $\Delta E_{\rm min} = -0.14 + 0.005 \cdot m_{K^+\pi^-}$, all in units of GeV, follow the variation of the ΔE resolution. We require $|\Delta E'| \leq 1$.

Continuum $e^+e^- \to q\bar{q}$ ($q = u, d, s, c$) events are the dominant background. To enhance discrimination between signal and continuum, we select events by using a neural network [30] with an output NN which combines three discriminating variables: the angles of the B momentum and the B thrust axis with respect to the e^+ beam direction in the CM frame, and the difference $2L_2 - L_0$ between two variables characterizing the energy flow about the B thrust axis. We have $L_n \equiv \sum_i p_i \cdot |\cos\theta_i|^n$, where the sum runs over all charged and neutral particles in the event (except for those in the B candidate) whose momenta $\vec{p}_i$ make angles θ_i with the B thrust axis. The neural network was trained on *off-resonance* data and correctly reconstructed signal Monte Carlo events. A data sample with about 4000 fully reconstructed $B^0 \to D^{*-}\pi^+$ decays with $D^{*-} \to \bar{D}^0\pi^-$ and $\bar{D}^0 \to K^+\pi^-$ is used to validate the shapes of the distributions on which the selection procedure is based.

Between 3% and 17% of the signal events have multiple reconstructed B candidates (usually two) depending on their location in the Dalitz plot. When distinct π^0 candidates make acceptable B combinations, we choose that with the reconstructed π^0 mass closest to the nominal value of 0.1349 GeV$/c^2$. When several acceptable B combinations can be made of distinct charged-particle sets, we arbitrarily choose one (in a reproducible fashion by using the date and time at which the event was recorded as a random number).

There are 8014 events in the data sample after the selection. The B meson candidate in each event is mass constrained to ensure that the measurement falls within the Dalitz-plot boundary. The resulting standard and square Dalitz plots are shown in Fig. 1. We now describe the composition of the selected data sample.

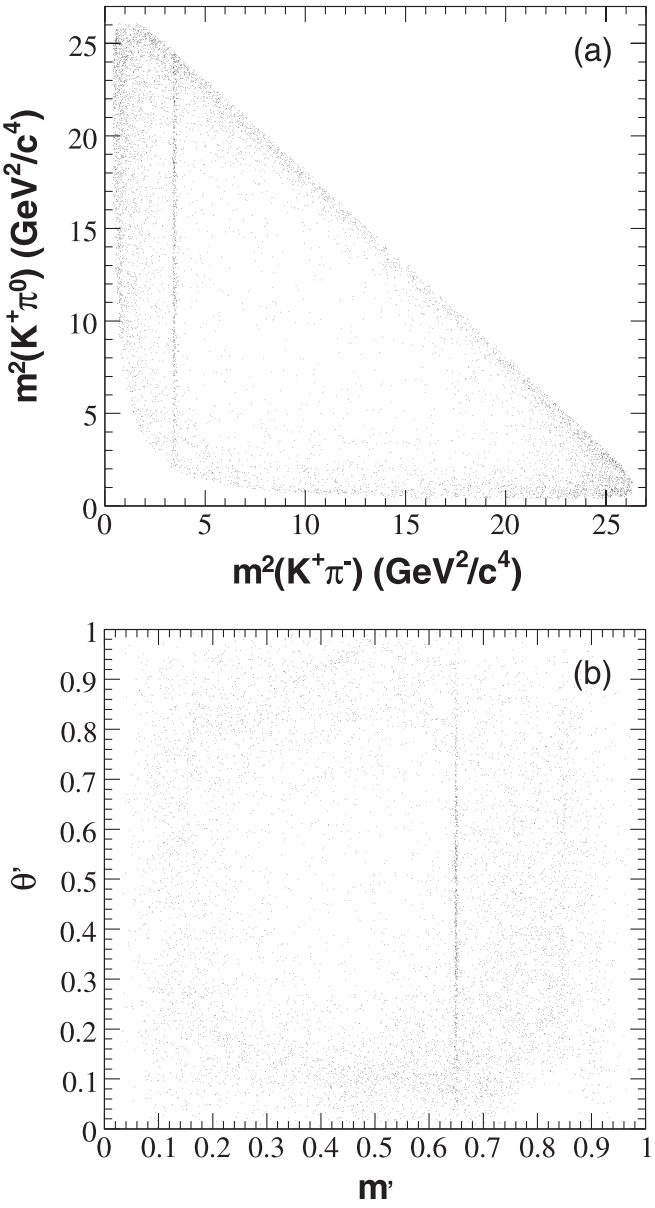

FIG. 1. The standard (a) and square (b) Dalitz plots of the selected data sample of 8014 events. The structures are more spread out in the square Dalitz plot. The $\bar{D}^0 \to K^+\pi^-$ narrow band is preserved with the choice made for the m' variable.

B. Truth-matched and self-cross-feed signal events

Using the Monte Carlo simulation as in [3], we distinguish between the correctly reconstructed and the misreconstructed signal events. A correctly reconstructed event, where the three particles of the B candidate match the generated ones, is called a *truth-matched* (TM) event. A misreconstructed signal event contains a B meson which decays to the signal mode, but one or more reconstructed particles in the B candidate are not actually from the decay of that B. A misreconstructed signal is called *self-cross-feed* (SCF). Misreconstruction is primarily due to the presence of low momentum pions. Consequently, the SCF

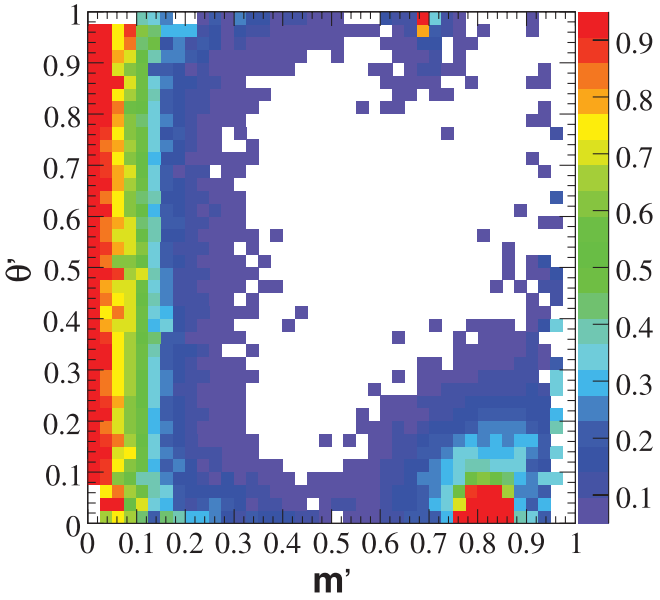

FIG. 2 (color). Fraction of misreconstructed events ($f_{\rm SCF}$), in the square Dalitz plot. This figure includes 4.9×10^6 signal Monte Carlo events. The white area is the SCF-free region.

TABLE II. Signal selection efficiencies (overall and truth-matched) and fraction of misreconstructed events (SCF) for different signal modes after full selection. As explained in the text, ε is the overall efficiency for (TM and SCF) signal events. Hence, $\varepsilon_{\rm TM} = \varepsilon(1 - f_{\rm SCF})$. The relative statistical precision on these numbers is a few tenths of a percent.

Decay mode	$\varepsilon(\%)$	$\varepsilon_{\rm TM}(\%)$	$f_{\rm SCF}(\%)$
$K^{*+}(892)\pi^-$	13.9	10.0	28.1
$K^+\rho^-$	14.3	10.3	28.3
$K^{*0}(892)\pi^0$	15.7	13.6	13.3
Nonresonant	16.2	15.2	6.2
$\bar{D}^0\pi^0$	16.4	15.7	4.0
D^-K^+	15.8	14.6	7.5

fraction varies across the Dalitz plot as shown in Fig. 2. For each point in the Dalitz plot, there is an efficiency $\varepsilon(m', \theta')$ to reconstruct an event either correctly or incorrectly. The quality of the reconstruction is poor where the SCF fraction $f_{\rm SCF}(m', \theta')$ is high. This occurs in the corners of the Dalitz plot where one of the final-state particles has a low momentum in the LAB frame. These variations can be seen in Fig. 2 and in Table II which compares efficiencies and $f_{\rm SCF}$ values averaged over the Dalitz plot for different $B^0 \to K^+\pi^-\pi^0$ subdecays[4] computed using high statistics Monte Carlo samples (4.9×10^6 $B^0 \to K^+\pi^-\pi^0$ events).

[4]We choose to classify the $B^0 \to \bar{D}^0\pi^0$, D^-K^+ subdecays as background since they proceed via a $b \to c$ quark-level transition while we are studying charmless processes.

It is important to keep a high efficiency in the Dalitz-plot corners where the low-mass vector resonances interfere. Overall, the total efficiency is close to 15%. The main sources of inefficiency are the $\Delta E'$ selection ($\varepsilon \approx$ 70%–80%), the kaon identification ($\varepsilon \approx 69\%$), and the neural network selection ($\varepsilon \approx 60\%$).

C. Background

1. Continuum background

Although the neural network selection rejects 96% of the continuum events, this background is the dominant class of events in the data sample, representing about two-thirds of its size.

2. Background from other B decays

Since there is no restriction on any two-body invariant mass of the final-state particles, large backgrounds from other B decays occur. We use high statistics Monte Carlo samples to study these backgrounds. Conservative assumptions about unknown branching fractions are made. For instance, when only an upper limit U is known for the branching fraction of a decay channel, we use $U/2 \pm U/2$ as an input to the simulation.

Inclusive and exclusive B decays with or without charm are grouped into ten classes to be used in the fit. Rates, and topological and kinematical similarities are studied to define the classes listed in Table III. There are two classes with inclusive $b \to c$ decays which are distinguished according to whether a genuine D^0 is part of the B candidate. We keep the exclusive decays $B^0 \to \bar{D}^0\pi^0$ with $\bar{D}^0 \to K^+\pi^-$ in the data sample because the copious yield of approximately 400 well-identified events helps to control the fit algorithm.

V. THE MAXIMUM LIKELIHOOD FIT

We perform an unbinned extended maximum likelihood fit to determine the total $B^0 \to K^+\pi^-\pi^0$ event yield, the magnitudes t_j, $\bar{t}_j$, and the phases ϕ_j, $\bar{\phi}_j$ of the complex isobar coefficients of the decay amplitude defined in Eqs. (1) and (2). The fit uses the variables m', θ', $m_{\rm ES}$, $\Delta E'$, and NN to discriminate signal from background.

A. The likelihood function

The selected on-resonance data sample is assumed to consist of signal, continuum background, and background from other B decays. Accordingly, the likelihood function of event i is written

$$\mathcal{L}_i = \mathcal{L}_{{\rm sig},i} + \mathcal{L}_{q\bar{q},i} + \sum_c \mathcal{L}_{B{\rm bg},c,i}, \qquad (20)$$

where the sum runs over all the B-background classes listed in Table III. All background likelihood functions have the same expression:

TABLE III. The list of B backgrounds retained for the fit (Sec. V). For each channel, we give (anticipating Sec. VI) either the fitted number of events in the data sample if its yield is allowed to vary in the fit procedure, or the expected number otherwise.

Class	Mode	Events	
0	$B^0 \to K^+\pi^-$	10.4 ± 0.5	Fixed
1	$B^0 \to K^{*0}(892)\gamma$, $K^{*0}(1430)\gamma$, $\rho^+\pi^-$	95.6 ± 5.0	Fixed
2	$B^0 \to \rho^+\rho^-$, $K^{*+}(892)\rho^-$, $K^*(1680)\rho$	10.7 ± 3.8	Fixed
3	$B^0 \to \bar{D}^0(K^+\pi^-)\pi^0$	424 ± 25	Varied
4	$B^+ \to K^+\pi^0$	17.4 ± 1.5	Fixed
5	$B^+ \to$ 3-body (mainly $K^+\pi^-\pi^+$)	119 ± 34	Fixed
6	$B \to$ 4-body	30.3 ± 3.4	Fixed
7	Generic $B \to$ charm without true D^0	382 ± 49	Varied
8	Generic $B \to$ charm with true D^0	147 ± 17	Varied
9	$B^0 \to D^-(\to \pi^-\pi^0)K^+$	20.4 ± 7.8	Fixed

TABLE IV. Summary of the PDF parametrizations. G = Gaussian, P1 = 1st order polynomial, NP = nonparametric, and CB = Crystal Ball. The notation GG(DP) designates a double Gaussian PDF with parameters which vary over the Dalitz plot. The Dalitz-plot signal model is described in Sec. II. The numbers associated with the B background in the last row are the class indices in Table III.

Component	m_{ES}	$\Delta E'$	NN	Dalitz
Signal (TM)	CB	GG(DP)	NP	See text
Signal (SCF)	NP	G	NP	See text
Continuum	ARGUS	P1	See text	NP in patches
B background (non-D)	Two-dim. NP		NP	NP
B background (3 and 9)	Signal-like	Signal-like	One NP for both	See text

$$\mathcal{L}_{\text{back},i} = N_{\text{back}}\tfrac{1}{2}(1 - q_i^K A_{\text{back}})\mathcal{P}_{\text{back},i}, \tag{21}$$

where q_i^K is the kaon charge in event i, and A_{back} is the charge asymmetry.

We consider B^0 and $\bar{B}^0$ separately to build the signal likelihood function.

$$N_{\text{sig}} = N_{\text{sig}}^+ + N_{\text{sig}}^-, \tag{22}$$

$$\mathcal{L}_{\text{sig},i} = \mathcal{L}_{\text{sig},i}^+ + \mathcal{L}_{\text{sig},i}^-. \tag{23}$$

Each part has two terms, one for the TM and one for the SCF events:

$$\begin{aligned}\mathcal{L}_{\text{sig},i}^+ &= \mathcal{L}_{\text{TM},i}^+ + \mathcal{L}_{\text{SCF},i}^+ \\ &= N_{\text{sig}}^+[(1 - \bar{f}_{\text{SCF}})\mathcal{P}_{\text{TM},i}^+ + \bar{f}_{\text{SCF}}\mathcal{P}_{\text{SCF},i}^+],\end{aligned} \tag{24}$$

and similarly for $\mathcal{L}_{\text{sig},i}^-$. $\bar{f}_{\text{SCF}}$, the fraction of SCF events averaged over the Dalitz plot, assumed to be the same for both flavors, is discussed below. We denote by N_{comp} the expected number of events for species *comp*. The fit maximizes the extended likelihood function[5]:

$$\mathcal{L} = e^{-N_{\text{tot}}}\prod_{i=1}^{N}\mathcal{L}_i, \tag{25}$$

where $N = 8014$ events is the size of the data sample and $N_{\text{tot}} = N_{\text{sig}} + N_{q\bar{q}} + \sum_c N_{B\text{bg},c}$ is the expected number of events.

The five-dimensional probability density functions (PDF) $\mathcal{P}$ are the products of the four PDFs of the measured discriminating variables $\upsilon = \{m_{\text{ES}}, \Delta E', \text{NN}, (m', \theta')\}$,

$$\mathcal{P} = \prod_{k=1}^{4}\mathcal{P}(\upsilon_k). \tag{26}$$

The correlations among the measurements are handled by building conditional PDFs where appropriate (between NN and the Dalitz variables for the continuum, and between $\Delta E'$ and the Dalitz variables for TM-signal events). Systematic uncertainties account for the correlations we neglect.

A total of 37 parameters are varied in the fit (see Sec. V D). A summary of the PDF parametrizations is given in Table IV.

[5]The canceling factors $1/N_{\text{tot}}$ in Eqs. (21) and (22), and N_{tot}^N in Eq. (25), required for the likelihood functions to be properly normalized, have been omitted for simplicity.

B. The Dalitz probability density functions

Since the decay $B^0 \to K^+\pi^-\pi^0$ is flavor specific (the charge of the kaon identifies the b flavor), the B^0 and $\bar{B}^0$ Dalitz plots are independent. However, because the backgrounds are essentially flavor blind, we get a more robust procedure by fitting them simultaneously. It is enough to describe only the B^0 Dalitz-plot PDF.[6] A change from $\mathcal{A}$ to $\bar{\mathcal{A}}$ [Eqs. (1) and (2)] gives the $\bar{B}^0$ PDF.

1. Signal

The signal Dalitz model has been described in Sec. II. The free parameters are the magnitudes and phases defined in Eqs. (1) and (2) for all the intermediate states of the signal model given in Table I. Since the measurement is done relative to the $K^{*+}(892)\pi^-$ final state, the phases of this and the charge conjugate channels are fixed to zero. The amplitude of $B^0 \to K^{*+}(892)\pi^-$ is also fixed but not that of $\bar{B}^0 \to K^{*-}(892)\pi^+$ in order to be sensitive to direct CP violation.

The normalization of the component signal PDFs:

$$\mathcal{P}_{\mathrm{TM},i} \propto \varepsilon_i(1 - f_{\mathrm{SCF},i})|\det\mathcal{J}_i||\mathcal{A}_i|^2, \tag{27}$$

$$\mathcal{P}_{\mathrm{SCF},i} \propto \varepsilon_i f_{\mathrm{SCF},i}[|\det\mathcal{J}||\mathcal{A}|^2 \otimes R_{\mathrm{SCF}}]_i, \tag{28}$$

is model dependent. $\mathcal{J}$ is the Jacobian matrix of the mapping to the square Dalitz plot. The symbol $\otimes$ stands for a convolution, and the R matrix is described below [Eq. (33)]. The normalization requires the computation of the integrals

$$\int_0^1 dm' \int_0^1 d\theta' \varepsilon(1 - f_{\mathrm{SCF}})|\det\mathcal{J}|f_k f_l^*, \tag{29}$$

$$\int_0^1 dm' \int_0^1 d\theta' \varepsilon f_{\mathrm{SCF}}|\det\mathcal{J}|f_k f_l^*, \tag{30}$$

and

$$\int_0^1 dm' \int_0^1 d\theta' \varepsilon|\det\mathcal{J}|f_k f_l^*, \tag{31}$$

where the notations of Eq. (1) are used. The integrations over the square Dalitz plot are performed numerically. The weight

$$\bar{f}_{\mathrm{SCF}} = \frac{\int_0^1 dm' \int_0^1 d\theta' \varepsilon f_{\mathrm{SCF}}|\det\mathcal{J}||\mathcal{A}|^2}{\int_0^1 dm' \int_0^1 d\theta' \varepsilon|\det\mathcal{J}||\mathcal{A}|^2} \tag{32}$$

in Eq. (22) ensures that the total signal PDF is normalized. The PDF normalization depends on the decay dynamics and is computed iteratively. In practice, the computation of $\bar{f}_{\mathrm{SCF}}$ rapidly converges to a value which we fix after a few exploratory fits.

Studies in simulation have shown that the experimental resolutions of m' and θ' need not be introduced in the TM-signal PDF. On the contrary, misreconstructed events often incur large migrations, when the reconstructed m'_r, θ'_r are far from the true values m'_t, θ'_t. We use the Monte Carlo simulation to compute a normalized two-dimensional resolution function $R_{\mathrm{SCF}}(m'_r, \theta'_r; m'_t, \theta'_t)$, with

$$\int_0^1 dm'_r \int_0^1 d\theta'_r R_{\mathrm{SCF}}(m'_r, \theta'_r; m'_t, \theta'_t) = 1. \tag{33}$$

R_{SCF} is convolved with the signal model in the expression of $\mathcal{P}_{\mathrm{SCF}}$ [Eq. (28)].

2. Background

Except for events coming from exclusive $B \to D$ decays, all background Dalitz PDF are nonparametric smoothed histograms. The continuum distributions are extracted from a combination of off-resonance data and a sideband $(5.20 < m_{\mathrm{ES}} < 5.25\ \mathrm{GeV}/c^2)$ of the on-resonance data from which the B background has been subtracted. The square Dalitz plot is divided into three regions where different smoothing parameters are applied in order to optimally reproduce the observed wide and narrow structures by using a two-dimensional kernel estimation technique [31]. For $m' > 0.8$ and all θ', a fine-grained model is needed to follow the peak from D^0 continuum production. For $m' < 0.8$ there are two different wide structures corresponding to the continuum production of the ρ's for θ' below 0.8 and the charged K^*'s above.

The B-background (Table III) Dalitz PDFs are obtained from the Monte Carlo simulation. For the components which model $b \to c$ decays with real D^0 mesons, a fine-grained binning around the D mass is used to construct the smoothed histograms. The exclusive signal-like components $B^0 \to \bar{D}^0\pi^0$, $\bar{D}^0 \to K^+\pi^-$ and $B^0 \to D^-K^+$, $D^- \to \pi^-\pi^0$ are modeled with TM-like and SCF-like PDFs. The former are products of a Gaussian distribution in $m_{K\pi}$ (then transformed into m') and a fifth order polynomial in θ'. The D^0 Gaussian mass and widths are free parameters in the fit, the TM-like D^0 helicity polynomial coefficients were obtained via an ancillary fit to the data, and all other parameters are fixed to their value in the Monte Carlo simulation. For the $B^0 \to D^-K^+$ where $D^- \to \pi^-\pi^0$, the Dalitz-plot PDF is a two-dimensional smoothed histogram obtained from the Monte Carlo simulation.

C. The other PDFs

1. Signal

The m_{ES} PDF for TM-signal events is a Crystal Ball function [32], the mean and width of which are free parameters in the fit. For SCF-signal events we use a nonparametric shape taken from the Monte Carlo simulation.

$\Delta E'$ is correlated with the Dalitz-plot variables for TM-signal events. To account for the correlation, we choose a double Gaussian PDF, the mean and standard deviation of which vary linearly with $m^2_{K^+\pi^-}$. These parameters (inter-

[6] We drop the superscript in $\mathcal{P}^+$ in the following.

cept and slope) are taken from the Monte Carlo simulation except for a global mean of the double Gaussian distribution. A wide single Gaussian distribution with mean and standard deviation taken from the Monte Carlo simulation is used for the SCF-signal $\Delta E'$ PDF.

The NN PDFs for TM and SCF events are nonparametric distributions taken from the Monte Carlo simulation.

2. Background

We use the ARGUS function [33]

$$f\left(z = \frac{m_{\rm ES}}{m_{\rm ES}^{\rm max}}\right) \propto z\sqrt{1-z^2}e^{-\xi(1-z^2)} \tag{34}$$

as the continuum $m_{\rm ES}$ PDF. The endpoint $m_{\rm ES}^{\rm max}$ and the shape parameter ξ are fixed to 5.2897 GeV/c^2 and -22, respectively ($\xi = -22 \pm 7$ from a fit to off-resonance data). The $\Delta E'$ PDF is a linear polynomial whose slope is free to vary in the fit. The shape of the NN distribution for the continuum is correlated with the event location in the Dalitz plot. To account for that effect we use for the NN PDF a function that varies with the closest distance $\Delta_{\rm Dalitz}$ between the point representing the event and the boundary of the standard Dalitz plot,

$$\mathcal{P}({\rm NN}; \Delta_{\rm Dalitz}) = (1 - {\rm NN})^A(B_0 + B_1{\rm NN} + B_2{\rm NN}^2). \tag{35}$$

The A and B coefficients are linear functions of $\Delta_{\rm Dalitz}$. Their expressions in terms of the a_i parameters that are varied in the likelihood fit are

$$\begin{aligned} A &= a_1 + a_4\Delta_{\rm Dalitz}, & B_0 &= c_0 + c_1\Delta_{\rm Dalitz}, \\ B_1 &= a_3 + c_2\Delta_{\rm Dalitz}, & B_2 &= a_2 + c_3\Delta_{\rm Dalitz}. \end{aligned} \tag{36}$$

We use two-dimensional nonparametric distributions to describe the B-background classes in the ($m_{\rm ES}$, $\Delta E'$) plane, except for the exclusive B decays to D mesons (classes 3 and 9) in Table III for which we use the same shapes as for the signal. For each B-background class the NN PDF is a nonparametric distribution taken from the Monte Carlo simulation. Classes 3 and 9 share the same NN PDF.

D. The fit parameters

The following parameters are varied in the fit:

(i) Five yields for signal ($N_{\rm sig}$), continuum ($N_{q\bar{q}}$), and three B-background classes ($c = 3$, 7, and 8 defined in Table III).
(ii) One CP asymmetry for the continuum events.
(iii) Four parameters related to narrow particle masses: the mass and mass resolution for the B^0 and the D^0.
(iv) Two parameters modeling the $\Delta E'$ distributions for the TM-signal events (global mean) and the continuum events (slope).
(v) Four parameters which account for the correlation between the NN output and the event location in the Dalitz plot [Eq. (36)].
(vi) Twenty-one isobar amplitudes and phases. There are six intermediate states (five resonances and a nonresonant term) and two Dalitz plots. We fix one reference amplitude, that of $B^0 \to K^{*+}(892)\pi^-$ and two phases for the latter and its conjugate. Therefore, we end up with 11 magnitudes and ten phases to be determined by the fit.

VI. RESULTS

The maximum likelihood fit results in a $B^0(\bar{B}^0) \to K^\pm\pi^\mp\pi^0$ event yield of $N_{\rm sig} = 1377 \pm 70$ events, where the uncertainty is statistical only. There are 5395 ± 104 continuum events and 424 ± 25 exclusive $B \to \bar{D}^0\pi^0$ decays where $\bar{D}^0 \to K^+\pi^-$ (not included in $N_{\rm sig}$). The remaining 833 B-background events are detailed in Table III.

When the fit is repeated starting from input parameter values randomly chosen within wide ranges of 1 order of magnitude above and below the nominal values for the amplitudes and within the $[0, 2\pi]$ interval for the phases, we observe convergence toward four solutions with minimum values of the negative loglikelihood function [NLL $\equiv -\log(\mathcal{L})$] that are equal within 0.2 units. There are four degenerate solutions. The event yields we quote are the averages of the four solutions for which the relative spreads are less than 1%. Monte Carlo (m', θ') scatter plots generated according to the fitted signal model in the four solutions are barely distinguishable. We checked with simulated data sets that multiple quasidegenerate solutions are to be expected when applying our fitting procedure to samples containing as many events as the experiment.

In the Appendix, the fitted parameters are given for the four solutions in Table IX, together with their correlation matrix (for solution I) in Tables X and XI. The isobar fractions, which are not required to sum to 1 in order to accommodate interference, are not significantly different from unity. We observe that the fit fractions and the CP asymmetries are consistent within less than 3 standard deviations among the solutions, and indeed agree much better for the subdecays to a pseudoscalar meson and a vector meson. The phases differ substantially. The four solutions are actually two solutions for the B^0 phases and two solutions for the $\bar{B}^0$ phases. The uncertainties and correlation coefficients given in these tables are statistical only. They are underestimated because the fitting program assumes a parabolic shape for the NLL in the vicinity of its minimum. This assumption overlooks the fit degeneracy. Before we explain how we derive consistent statistical and systematic uncertainties, we proceed to describe the goodness of the fit. We postpone the discussion of the physical meaning of the fitted signal model to Sec. VIII.

To check the validity of the fits and to study the results, we have generated 1000 pseudoexperiments with as many

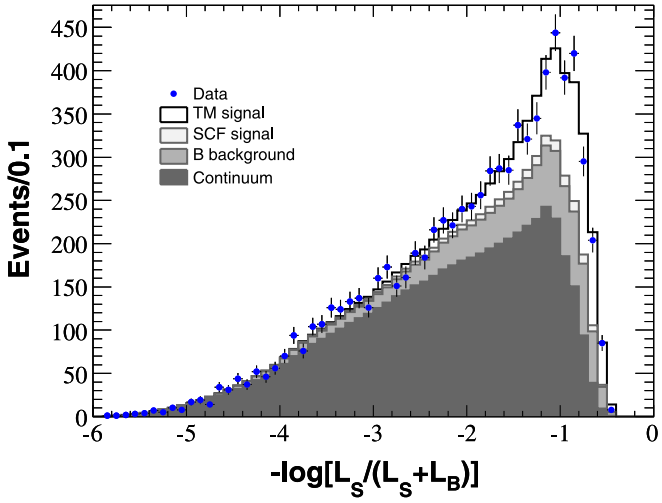

FIG. 3 (color online). Ratio of the TM term $\mathcal{L}_{\mathrm{TM},i}$ [first relevant term in Eq. (22)] over the full likelihood function $\mathcal{L}_i$ [Eq. (20)] for all events. The data are shown as points with error bars. The solid histogram shows the projection of the fit result. The dark and gray shaded areas represent the continuum and B background, respectively. The light gray region shows the SCF contribution.

events as in the data sample using PDFs with the fitted parameter values. We check that the NLL of the experimental fit falls well within the NLL distribution in the pseudoexperiments. The goodness of the fits and their ability to reproduce the real data are similar for all four solutions. We show the results of solution I in the following. We compare the likelihood ratio $r_{\mathrm{lik}} \equiv \frac{\mathcal{L}_{\mathrm{TM}}}{\mathcal{L}}$ [see Eqs. (20) and (24)] in the data and in the pseudoexperiments and see good agreement (Fig. 3). The distributions of the discriminating variables (m_{ES}, $\Delta E'$, and NN) are shown in Fig. 4 for samples that have been enriched in signal events by restricting r_{lik} (computed without the plotted variable) to large enough values in order to maximize the signal significance.

Figure 5 shows the Dalitz-plot mass spectra over their full range with no restriction on r_{lik}. A zoom of the low-mass resonance region (below 1.75 GeV/c^2) is shown for signal-enriched events in Fig. 6. More details are shown in Fig. 7 (Fig. 8) which displays $m_{K^+\pi^-}$ ($m_{K^+\pi^0}$) for different intervals of the helicity angles $\theta_{K^+\pi^-}$ ($\theta_{K^+\pi^0}$). The interference between the scalar and vector K^* is evident from the opposite sign of the forward-backward helicity asymmetries below and above the $K^*(892)$. This effect is seen with sufficient statistics in these plots which include both B^0 and $\bar{B}^0$ decays, because the measured phase differences are similar in both cases (Table IX).

We take into account all four solutions of the fit to quote the final results of the analysis. To determine the statistical uncertainty on a physical parameter p, we fix it at successive values, spanning its range of interest, and repeat the fit, maximizing the projected likelihood function [Eq. (25)

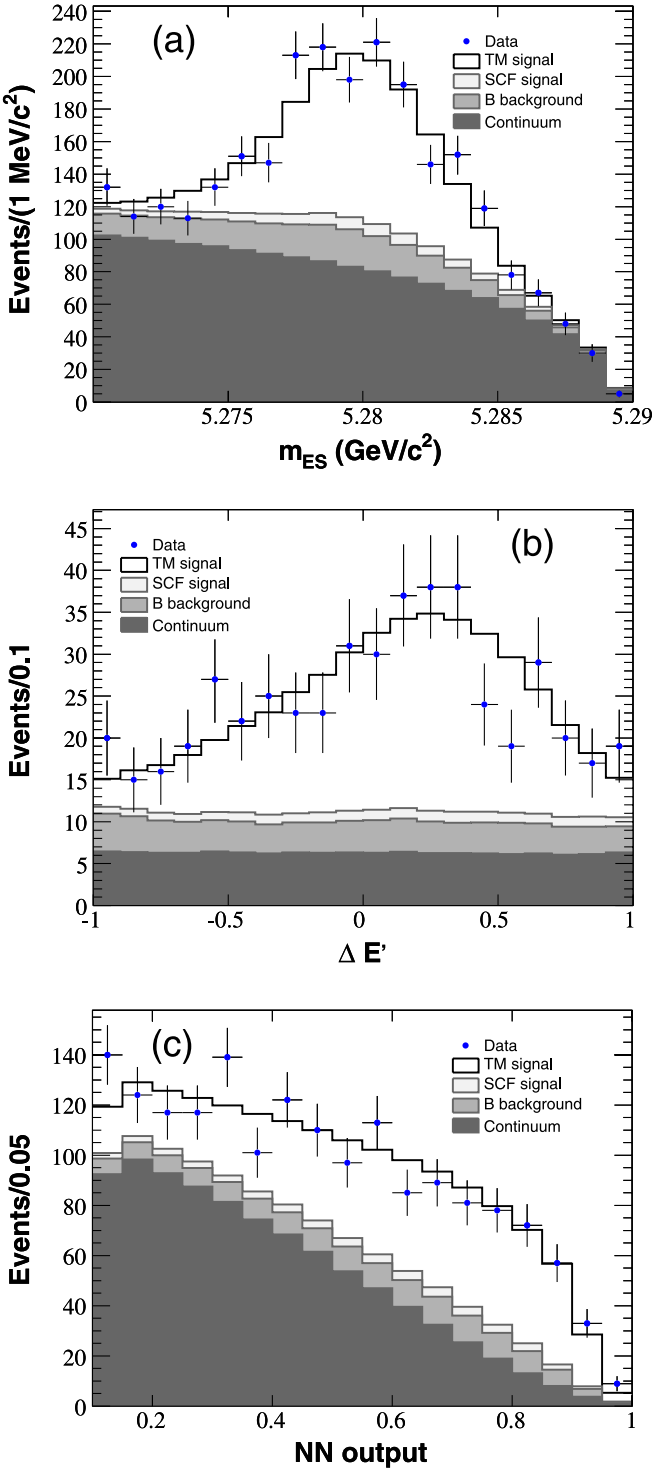

FIG. 4 (color online). (a) m_{ES}, (b) $\Delta E'$, and (c) NN distributions after restricting r_{lik} to enhance signal. The fractions of accepted signal and rejected continuum events are, respectively, 65% and 71% (a), 21% and 97% (b), and 49% and 83% (c). The data are shown as points with error bars. The solid histogram shows the projection of the fit result. The dark and gray shaded areas represent the continuum and B background, respectively. The light gray region shows the SCF contribution.

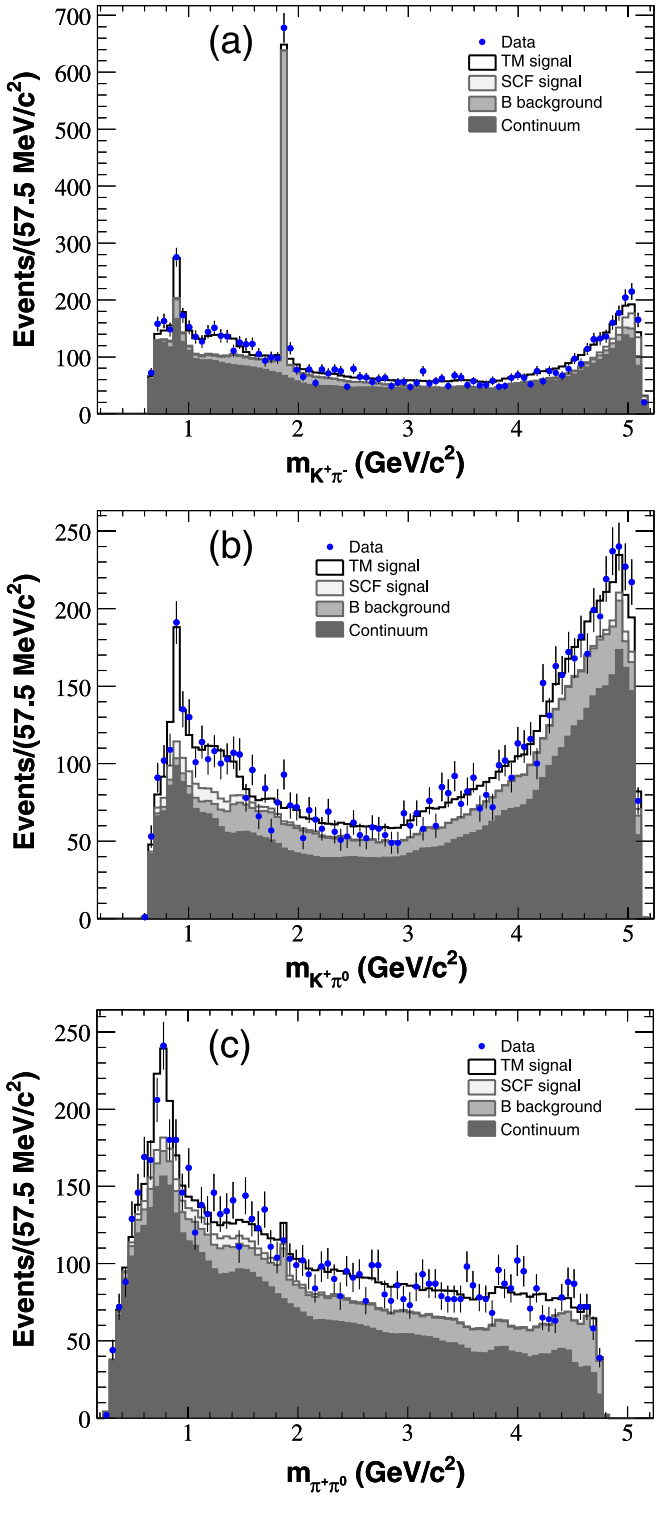

FIG. 5 (color online). The invariant mass spectra for all events: $m_{K^+\pi^-}$ (a), $m_{K^+\pi^0}$ (b), and $m_{\pi^-\pi^0}$ (c). The data are shown as points with error bars. The solid histogram shows the projection of the fit result. The dark and gray shaded areas represent the continuum and B background, respectively. The light gray region shows the SCF contribution. The $\bar{D}^0$ mass peak is prominent in the top plot.

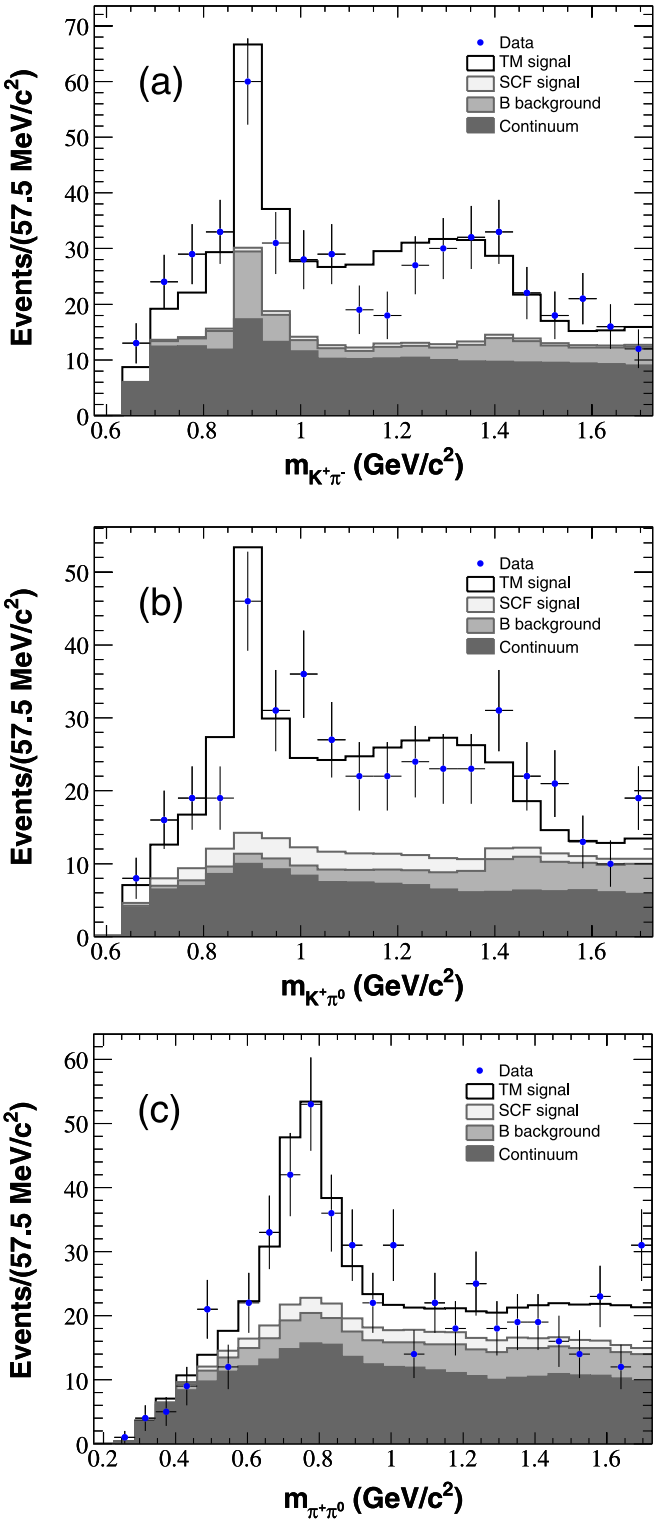

FIG. 6 (color online). The signal-enriched spectra for masses between threshold and 1.75 GeV/c^2: $m_{K^+\pi^-}$ (a), $m_{K^+\pi^0}$ (b), and $m_{\pi^-\pi^0}$ (c). The fractions of accepted signal and rejected continuum events are, respectively, 51% and 89%. The data are shown as points with error bars. The solid histogram shows the projection of the fit result. The dark and gray shaded areas represent the continuum and B background, respectively. The light gray region shows the SCF contribution.

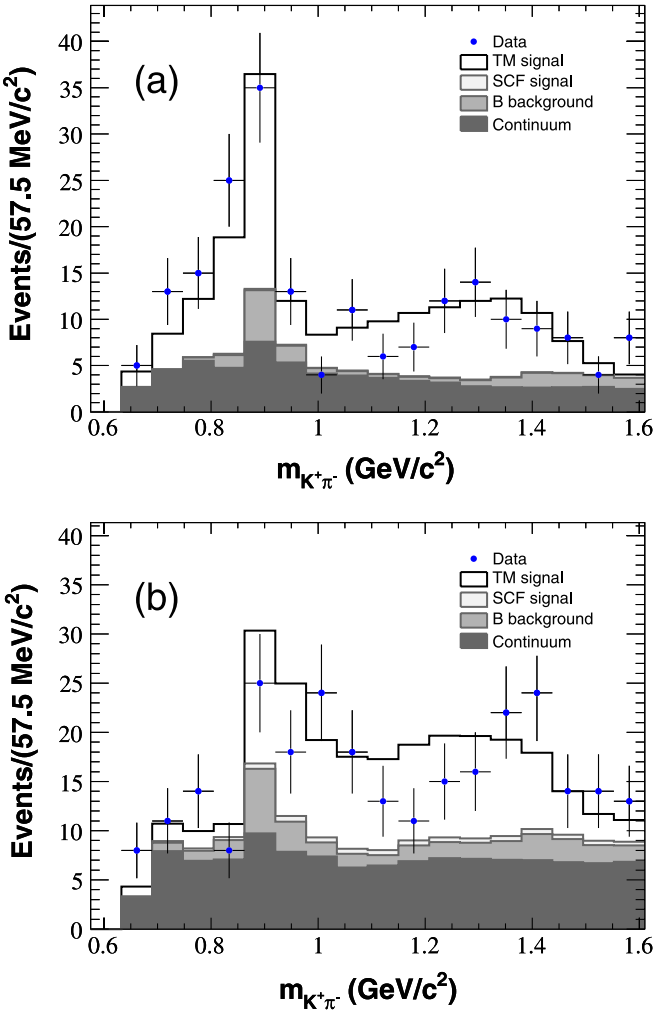

FIG. 7 (color online). Signal-enriched spectra of $m_{K^+\pi^-}$ in the low-mass resonance region and different ranges of the helicity angle, $\theta_{K^+\pi^-}$. (a) $0 < \theta_{K^+\pi^-} < 90$ degrees, (b) $90 < \theta_{K^+\pi^-} < 180$ degrees. The data sample is enriched in signal events as in Fig. 6. An interference between the vector and scalar K^{*0} is apparent through a positive forward-backward asymmetry below the $K^*(892)$ and a negative one above. The data are shown as points with error bars. The solid histogram shows the projection of the fit result. The dark and gray shaded areas represent the continuum and B background, respectively. The light gray region shows the SCF contribution.

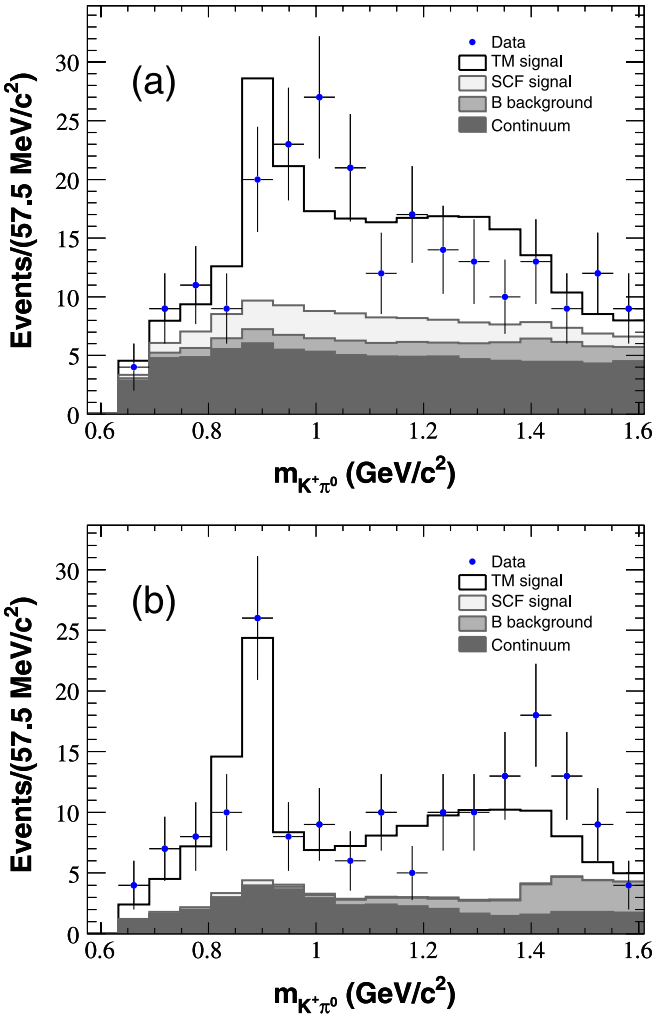

FIG. 8 (color online). Signal-enriched spectra of $m_{K^+\pi^0}$ in the low-mass resonance region and different ranges of the helicity angle, $\theta_{K^+\pi^0}$. (a) $0 < \theta_{K^+\pi^0} < 90$ degrees, (b) $90 < \theta_{K^+\pi^0} < 180$ degrees. The data sample is enriched in signal events as in Fig. 6. An interference between the vector and scalar K^* is apparent through a negative forward-backward asymmetry below the $K^*(892)$ and a positive one above. The data are shown as points with error bars. The solid histogram shows the projection of the fit result. The dark and gray shaded areas represent the continuum and B background, respectively. The light gray region shows the SCF contribution.

where p is frozen]. NLL(p), the minimum where the fit converges given p, is not always associated with the same solution. Therefore the NLL(p) envelope curve is far from a parabola. The flatness of its shape around the overall minimum reflects the fit degeneracy. The parameter values at which $\Delta\chi^2 \equiv 2(\mathrm{NLL} - \mathrm{NLL}_{\mathrm{best\ fit}})$ reaches unity bound the 1 standard deviation confidence interval. The scan of the $K^{*0}(892)\pi^0$ isobar fraction is shown in Fig. 9. The graph also shows the envelope curve obtained when the systematic uncertainty is included. The null value of the branching fraction is excluded with a statistical and systematic significance of 5.6 standard deviations. Thus, this is the first observation of the decay $B^0 \to K^{*0}(892)\pi^0$. Other scans are presented in the Appendix.

VII. SYSTEMATIC UNCERTAINTIES

Many fits neighboring the nominal fit are tried to study the dominant systematic effects which are summarized in Table V. For each parameter of interest p (FF, A_{CP}, ϕ), the positive (negative) deviations from each effect are summed in quadrature to obtain total upward (downward) systematic errors δp_+ (δp_-). The total projected likelihood function $\mathcal{L}_{\mathrm{tot}}(p)$ is computed as the convolution of the fit

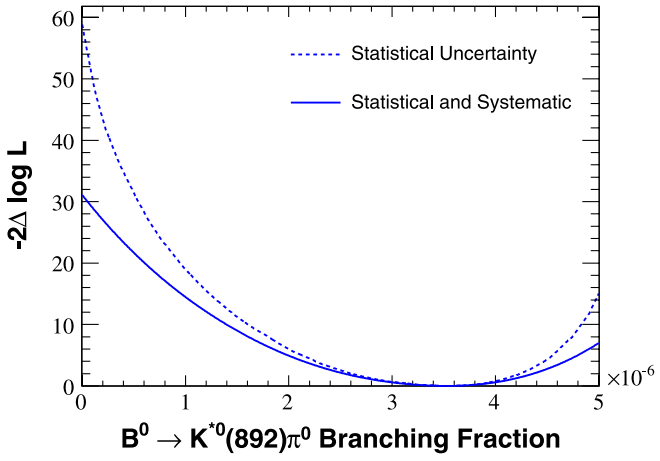

FIG. 9 (color online). The NLL close to its minimum as a function of the $K^{*0}(892)\pi^0$ branching fraction. The shapes of the curves are nonparabolic and shallow because the plotted $\Delta\chi^2$ is the smallest of those from all solutions. The dashed line scan corresponds to the statistical uncertainty. The solid line is the scan after smearing by the systematic uncertainties described in Sec. VII.

projected likelihood function defined at the end of the previous section, by a bifurcated Gaussian distribution with a lower (upper) standard deviation δp_- (δp_+). The scan of $\mathcal{L}_{\rm tot}$ drawn as a solid line on Fig. 9 (and subsequent ones) is used to determine the total confidence interval which accounts for both statistical and systematic uncertainties. Finally, the upward (downward) systematic uncertainty on p (Table VI) is the quadratic difference between the upward (downward) limits of the total and statistical confidence intervals. Note that when p central values significantly differ between the four fit solutions, the lowest $p_{\rm min}$ and highest $p_{\rm max}$ are used in the determination of the downward (upward) uncertainties, and an additional systematic uncertainty $\pm(p_{\rm max} - p_{\rm min})/2$ is quoted in Table VI.

While simple methods can be used to estimate the systematic effects on the isobar fractions and CP asymmetries, it is often necessary to estimate upper limits for phases. In such cases (the rows labeled *Other* in Table V) we conservatively use the upper limits at the 90% confidence level as the systematic uncertainties.

To estimate the contribution of other resonances, we fit the on-resonance data with extended signal models including one *extra* resonance on top of those in the nomin al signal model. The $\rho^-(1450)K^+$, $\rho^-(1700)K^+$, $K_2^{*0}(1430)\pi^0$, $K_2^{*+}(1430)\pi^-$, $K^{*0}(1680)\pi^0$, and $K^{*+}(1680)\pi^-$ final states have been studied. These fits are not significantly better than the nominal fit. The isobar fractions of all extra resonances are below 5%. None is significant. The isobar fractions of the nominal resonances change by nonsignificant amounts which we record as (*Dalitz-plot model*) systematic uncertainties in Table V. Changes in A_{CP} are also recorded. As we explain in Sec. VIII our fitting procedure is sensitive to some phase differences but not others. When there is sensitivity, the systematic Dalitz-plot model effects are insignificant. When there is no sensitivity, dramatic deviations occur. However, since these phase differences are essentially undetermined by the fit, we do not record these changes as systematic effects. Note that we have not included the low-mass κ resonance which is not established, as it is an alternative to the $(K\pi)_0^{*0}$ isobar from the model. In a further study, it has been shown that adding it to the model results in a destructive interference with the latter state, an insignificant κ amplitude, and no change in the $K^{*0}(892)\pi^0$ numeric results.

There are fixed parameters in the nominal fit model. We estimate the associated (*Shape parameters and B background*) systematic uncertainties by repeating the fit giving the studied parameter values at ± 1 standard deviation from its fixed value or at the limits of a conservative range. The fixed parameters to which the isobar fractions are sensitive are $\bar{f}_{\rm SCF}$ [Eq. (32)] and the $\Delta E'$-signal PDF parameters. $\bar{f}_{\rm SCF}$ was varied between 10% and 16%, a range that is inferred from the comparison of the data and simulation of $B \to D\rho$ events as explained in Refs. [3,34]. The A_{CP} mainly depend on the fixed CP asymmetries of B-background classes 1 and 7 (see Table III). We vary them by ± 0.5 and ± 0.2 to determine the (*B-background*) systematic uncertainties. These intervals were chosen after inspection of the latest available measurements [35].

The variations of the physical parameters of the resonances in the nominal signal model are recorded as (*Line shape*) systematic uncertainties. In particular, variations of the barrier coefficients R in Eq. (8) cause no significant effects.

The method used to determine the continuum square Dalitz-plot PDF (Sec. V B) has been extensively tested in the Monte Carlo simulation. The spread of the yields across those tests is used to estimate the associated (*Continuum DP PDF*) systematic errors. Among the dominant effects is the variation of the distortion of the Dalitz-plot distribution as a function of $m_{\rm ES}$ due to the B meson mass constraint.

To estimate the *Fit bias* uncertainties stemming from the imperfection of the fit model [most importantly, the too simple description of the SCF but also the neglected correlations between $m_{\rm ES}$ and $\Delta E'$ for TM-signal and B-background events, and the neglected resolution effect smearing the $K^{*\pm}(892)$ peak], we record the fitted biases and spreads in fits performed on large Monte Carlo samples with GEANT4 signal events and the actual amount of background generated along with their PDFs. Since the SCF prevails in the Dalitz-plot corners where the resonances interfere, this kind of systematic uncertainty is the dominant one for the phase measurements.

For the B meson branching fraction measurements, we have to include additionally the effect of imperfections in the event reconstruction on the efficiency. Adding in quad-

TABLE V. Summary of the systematic uncertainties. The systematic uncertainties are equal for the phases ϕ and $\bar{\phi}$. All phases ϕ are referenced to $\phi_{K^{*+}(892)\pi^-}$ and $\bar{\phi}$ to $\phi_{K^{*-}(892)\pi^+}$. The systematic uncertainties associated with the Dalitz-plot model and the line shapes are negligible for the phases of the $K\pi$ S-waves which are the only phase angles that are measured with some statistical accuracy. For the others, which are essentially undetermined by the fit, we do not quote these *undefined* systematic uncertainties.

		Fraction (%)	A_{CP}	ϕ (deg.)
$K^{*+}(892)\pi^-$	Dalitz-plot model	± 0.32	± 0.03	$\cdots$
	Shape parameters	$^{+0.31}_{-0.34}$	$^{+0.01}_{-0.02}$	$\cdots$
	B background	$^{+0.06}_{-0.14}$	± 0.02	$\cdots$
	Line shapes	$^{+0.06}_{-0.04}$	± 0.001	$\cdots$
	Continuum DP PDF	± 0.31		$\cdots$
	Fit bias	± 0.23	± 0.01	$\cdots$
	Total	$^{+0.59}_{-0.62}$	± 0.04	$\cdots$
$K^{*0}(892)\pi^0$	Dalitz-plot model	± 0.11	± 0.04	Undefined
	Shape parameters	$^{+0.30}_{-0.20}$	$^{+0.03}_{-0.02}$	
	B background	$^{+0.19}_{-0.15}$	$^{+0.07}_{-0.08}$	
	Line shapes	$^{+0.01}_{-0.02}$	± 0.001	Undefined
	Continuum DP PDF	± 0.49		± 6.3
	Fit bias	± 0.24	± 0.01	± 16.5
	Other			± 4.1
	Total	$^{+0.66}_{-0.61}$	± 0.09	± 18.2
$(K\pi)_0^{*+}\pi^-$	Dalitz-plot model	± 1.56	± 0.07	
	Shape parameters	$^{+1.14}_{-0.91}$	± 0.01	
	B background	$^{+0.32}_{-0.28}$	± 0.05	
	Line shapes	$^{+0.02}_{-0.04}$	± 0.000	
	Continuum DP PDF	± 0.82		± 2.6
	Fit bias	± 0.10	± 0.01	± 9.6
	Other			± 1.5
	Total	$^{+2.12}_{-2.00}$	± 0.09	± 10.1
$(K\pi)_0^{*0}\pi^0$	Dalitz-plot model	± 2.81	± 0.09	
	Shape parameters	$^{+2.30}_{-0.57}$	$^{+0.08}_{-0.03}$	
	B background	$^{+0.40}_{-0.46}$	$^{+0.04}_{-0.05}$	
	Line shapes	$^{+0.05}_{-0.06}$	± 0.002	
	Continuum DP PDF	± 0.73		± 5.2
	Fit bias	± 0.19	± 0.01	± 14.5
	Other			± 4.4
	Total	$^{+3.73}_{-3.00}$	$^{+0.13}_{-0.11}$	± 16.0
$\rho(770)^-K^+$	Dalitz-plot model	± 0.98	± 0.04	Undefined
	Shape parameters	$^{+0.34}_{-0.43}$	± 0.01	
	B background	$^{+0.17}_{-0.25}$	± 0.05	
	Line shapes	$^{+0.04}_{-0.03}$	± 0.001	Undefined
	Continuum DP PDF	± 0.45		± 3.6
	Fit bias	± 0.15	± 0.01	± 13.7
	Other			± 2.6
	Total	$^{+1.15}_{-1.19}$	± 0.07	± 14.4
NR	Dalitz-plot model	± 0.41	± 0.04	Undefined
	Shape parameters	$^{+0.46}_{-0.51}$	± 0.04	
	B background	$^{+0.64}_{-0.24}$	$^{+0.10}_{-0.08}$	
	Line shapes	$^{+0.04}_{-0.03}$	± 0.001	Undefined
	Continuum DP PDF	± 0.91		± 5.8
	Fit bias	± 0.22	± 0.01	± 6.8
	Other			± 2.6
	Total	$^{+1.29}_{-1.17}$	$^{+0.11}_{-0.10}$	± 9.3

TABLE VI. Final results for rates and CP asymmetries. The quasi-two-body branching fractions $\mathcal{B}_j$ have been computed from the isobar fractions FF_j using Eq. (15). The statistical uncertainties are given first. The statistical and systematic uncertainties are calculated by scanning the NLL close to its minimum, taking into account the four fit solutions and recording the values where the NLL increases by one unit above its minimum. For the final states with $K\pi$ S-waves, a second systematic uncertainty covers the spread between the best fit values from the four solutions. For resonances that are considered in extended fit models, we quote upper limits at the 90% confidence level (based on statistical uncertainties only) for the isobar fractions and the quasi-two-body branching fractions.

Isobar j	FF_j (%)	$\mathcal{B}_j$ (10^{-6})	A_{CP}^j
$K^{*+}(892)\pi^-$	$11.8^{+2.5}_{-1.5} \pm 0.6$	$4.2^{+0.9}_{-0.5} \pm 0.3$	$-0.19^{+0.20}_{-0.15} \pm 0.04$
$K^{*0}(892)\pi^0$	$6.7^{+1.3+0.7}_{-1.5-0.6}$	$2.4 \pm 0.5 \pm 0.3$	$-0.09^{+0.21}_{-0.24} \pm 0.09$
$(K\pi)_0^{*+}\pi^-$	$26.3^{+3.1+2.1}_{-3.8-2.0} \pm 4.9$	$9.4^{+1.1+1.4}_{-1.3-1.1} \pm 1.8$	$+0.17^{+0.11}_{-0.16} \pm 0.09 \pm 0.20$
$(K\pi)_0^{*0}\pi^0$	$24.3^{+3.0+3.7}_{-2.6-3.0} \pm 6.7$	$8.7^{+1.1+1.8}_{-0.9-1.3} \pm 2.2$	$-0.22 \pm 0.12^{+0.13}_{-0.11} \pm 0.27$
$\rho^-(770)K^+$	$22.5^{+2.2}_{-3.7} \pm 1.2$	$8.0^{+0.8}_{-1.3} \pm 0.6$	$+0.11^{+0.14}_{-0.15} \pm 0.07$
NR	$12.4 \pm 2.6^{+1.3}_{-1.2}$	$4.4 \pm 0.9 \pm 0.5$	$+0.23^{+0.19+0.11}_{-0.27-0.10}$
Total	$102.3^{+7.1}_{-4.0} \pm 4.1$	$35.7^{+2.6}_{-1.5} \pm 2.2$	$-0.030^{+0.045}_{-0.051} \pm 0.055$
	FF_j, [Upper Limits] (%)	Upper Limits (10^{-6})	
$\rho^-(1450)K^+$	$2.2^{+2.2}_{-1.5}$, [5.9]	2.1	
$\rho^-(1700)K^+$	$0.7^{+1.2}_{-0.6}$, [3.1]	1.1	
$K_2^{*0}(1430)\pi^0$	$1.2^{+1.5}_{-1.0}$, [3.6]	1.3	
$K_2^{*+}(1430)\pi^-$	$5.2^{+1.6}_{-1.4}$, [7.5]	2.7	
$K^{*0}(1680)\pi^0$	$3.0^{+1.6}_{-1.3}$, [5.5]	2.0	
$K^{*+}(1680)\pi^-$	$5.7^{+2.0}_{-1.7}$, [8.9]	3.2	

TABLE VII. Final results for phases. When there is sensitivity, the results are the 1 standard deviation confidence interval (1σ c.i.) for the phase angle measurements (in degrees). The statistical and systematic uncertainties, determined by the NLL scan method described in Fig. 9, are included. The interval bounds can be seen on the graphs referenced in the second column, as the intersections of the solid scan curves with the ($\Delta\chi^2 = 1$) horizontal dashed lines. The $\Delta\chi^2$ evaluated for zero $\delta\phi$ measures the significance (squared) for direct CP violation. When there is no sensitivity, we give the maximum $\Delta\chi^2$ reached over the scanned region.

Interference pattern	Graph	Results	$\Delta\phi$ for B^0	$\Delta\bar{\phi}$ for $\bar{B}^0$	$\delta\phi \equiv \Delta\bar{\phi} - \Delta\phi$	$\Delta\chi^2(\delta\phi = 0)$
$K\pi$ neutral-charged P-waves	Figure 10	$\Delta\chi^2_{\max}$	2.2	5.4	0.88	
$K\pi$ neutral-charged S-waves	Figure 11	$\Delta\chi^2_{\max}$	2.2	7.6	0.84	
$\rho^{\mp}K^{\pm} - K^{*\pm}\pi^{\mp}$	Figure 14	$\Delta\chi^2_{\max}$	7.6	1.9	1.0	
Charged $K\pi$ P-wave–S-wave	Figure 12	1σ c.i.	[177, 209]	[232, 305]	[44, 116]	3.1
Neutral $K\pi$ P-wave–S-wave	Figure 13	1σ c.i.	$[-6, 41]$	$[-12, 46]$	$[-32, 38]$	0
NR-charged S-waves	Figure 15	1σ c.i.	$[-87, -41]$ $[20, 81]$	$[-84, 38]$	$[-151, 107]$	0
NR-neutral S-waves	Figure 16	1σ c.i.	$[-96, -41]$ $[-3, 75]$	$[-84, 67]$	$[-145, 145]$	0

rature the uncertainties associated with tracking (1.6%), charged-particle identification (2%), π^0 reconstruction (3%), the efficiency of the selection requirements (0.3% for $m_{\rm ES}$, 1.2% for ΔE, 2% for the NN), and the integrated luminosity (1.1%), we obtain a global systematic percent error of 4.7%.

VIII. INTERPRETATION

The final results are given in Tables VI, VII, and VIII. The total branching fraction $\mathcal{B}(B^0 \to K^+\pi^-\pi^0) = (35.7^{+2.6}_{-1.5} \pm 2.2) \times 10^{-6}$ and the global CP asymmetry $\mathcal{A}_{CP} = -0.030^{+0.045}_{-0.051} \pm 0.055$ are compatible with the published measurements from Belle [11], $(36.6^{+4.2}_{-4.3} \pm 3.0) \times 10^{-6}$ and $0.07 \pm 0.11 \pm 0.01$, respectively. The decay[7] $B^0 \to K^{*0}(892)\pi^0$ is observed with a significance of 5.6 standard deviations (including systematics). We measure $\mathcal{B}(B^0 \to K^{*0}(892)\pi^0) = (3.6 \pm 0.7 \pm 0.4) \times 10^{-6}$,

[7]Isospin conservation is assumed for the strong decays of an $I = 1/2$ K meson resonance k^* to $K\pi$ when we compute the branching fraction of the quasi-two-body process $B^0 \to k^*\pi$, namely, $\frac{\Gamma(k^{*0}\to K^+\pi^-)}{\Gamma(k^{*0}\to K\pi)} = 2/3$, and $\frac{\Gamma(k^{*+}\to K^+\pi^0)}{\Gamma(k^{*+}\to K\pi)} = 1/3$.

TABLE VIII. The branching fractions $\mathcal{B}$ of B decays to quasi-two-body final states assuming that all K^* resonances are isospin-1/2 states. The branching fractions of the $K_2^*(1430)$ and $K^*(1680)$ resonances to $K\pi$ from Ref. [24] have been used. The upper limits at 90% confidence level, $\mathcal{UL}$, are based on statistical uncertainties only.

B decay final state	$\mathcal{B}$ (10^{-6})
$K^{*+}(892)\pi^-$	$12.6^{+2.7}_{-1.6} \pm 0.9$
$K^{*0}(892)\pi^0$	$3.6 \pm 0.7 \pm 0.4$
$(K\pi)_0^{*+}\pi^-$; $(K\pi)_0^{*+} \to K^+\pi^0$	$9.4^{+1.1+1.4}_{-1.3-1.1} \pm 1.8$
$(K\pi)_0^{*0}\pi^0$; $(K\pi)_0^{*0} \to K^+\pi^+$	$8.7^{+1.1+1.8}_{-0.9-1.3} \pm 2.2$
$\rho^-(770)K^+$	$8.0^{+0.8}_{-1.3} \pm 0.6$
NR	$4.4 \pm 0.9 \pm 0.5$
	$\mathcal{UL}$ (10^{-6})
$\rho^-(1450)K^+$	2.1
$\rho^-(1700)K^+$	1.1
$K_2^{*0}(1430)\pi^0$	4.0
$K_2^{*+}(1430)\pi^-$	16.2
$K^{*0}(1680)\pi^0$	7.5
$K^{*+}(1680)\pi^-$	25

just at the edge of the 90% upper limits of previous experiments (3.5×10^{-6} by Belle [11] and 3.6×10^{-6} by CLEO [12]) combined with 3.5×10^{-6} in Ref. [24]. The subdecay branching fraction for $B^0 \to K^{*+}(892)\pi^-$ agrees with previous measurements from Belle [11,17] and *BABAR* [16] in both $K^{*+} \to K^+\pi^0$ and $K_S^0\pi^+$ decay channels. Averaging the *BABAR* measurements, one obtains $\mathcal{B}(B^0 \to K^{*+}(892)\pi^-) = (11.7^{+1.3}_{-1.2}) \times 10^{-6}$ and $A_{CP}(B^0 \to K^{*+}(892)\pi^-) = -0.14 \pm 0.12$. The branching fraction for $B^0 \to \rho^- K^+$ is lower than those measured by Belle [11] and CLEO [12] but in agreement within errors. If we assume that the $(K\pi)_0^{*+,0}$ isobars are pure isospin-1/2 and neglect possible non-$K\pi$ final states, we determine the following effective branching fractions: $\mathcal{B}(B^0 \to (K\pi)_0^{*+}\pi^-) = (28.2^{+3.3+4.3}_{-4.1-3.3} \pm 5.2) \times 10^{-6}$ and $\mathcal{B}(B^0 \to (K\pi)_0^{*0}\pi^0) = (13.1^{+1.6+2.7}_{-1.5-1.9} \pm 3.6) \times 10^{-6}$. A consistency check of our analysis is provided by our measurement of the branching ratio, $\mathcal{B}(B^0 \to \bar{D}^0\pi^0) = (2.93 \pm 0.17 \pm 0.18) \times 10^{-4}$, in agreement with its world average and that of the branching fraction of the decay $D^0 \to K^-\pi^+$ [24].

There is no evidence of direct CP violation in any resonant subdecay. In Tables VI and VIII we give upper limits at the 90% statistical confidence level on the branching fractions of resonances that might contribute to $K^+\pi^-\pi^0$ but are not part of the nominal signal model.

We also search for direct CP violation in the interference between pairs of isobars (R_i, R_j) by comparing the interference patterns in the B^0 and $\bar{B}^0$ Dalitz plots. In the figures described in this section, we display three NLL scans for, in turn, $\Delta\phi_{ij} \equiv \phi_j - \phi_i$, the phase difference between the

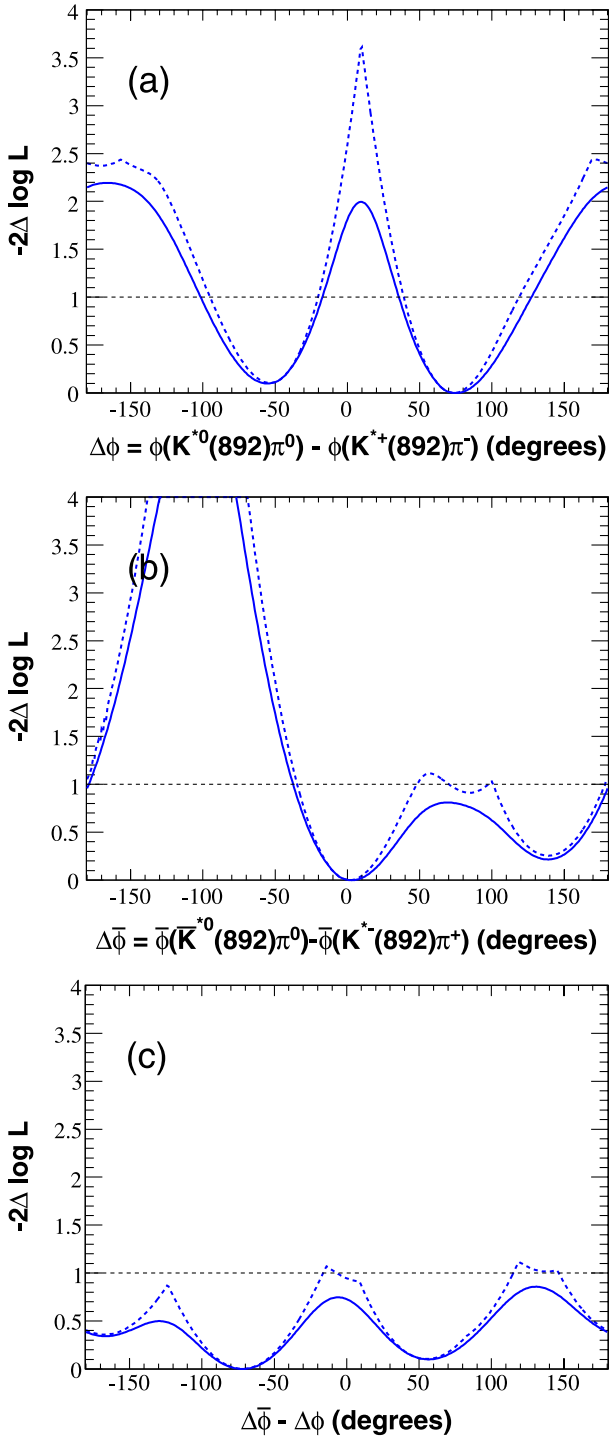

FIG. 10 (color online). The phase difference between the K^{*0} and the charged K^* for the P-wave $K^*(892)$. The three diagrams are the NLL scans for the B^0 (a) and $\bar{B}^0$ (b) decays as well as their differences (c). The dashed line gives the statistical uncertainty, and the solid line, the total uncertainty. The data do not indicate preferred angles, except for the $[-131, -75]$ degree range which is excluded for $\bar{B}^0$ at the 2 standard deviation level. The four fit solutions find their NLL minimum for distinct phases. The vertical scale stops at $2\Delta(\text{NLL}) = 4$ slightly above 3.84 which is the 95% confidence level. A horizontal dashed line at $2\Delta(\text{NLL}) = 1$ shows the 1 standard deviation level.

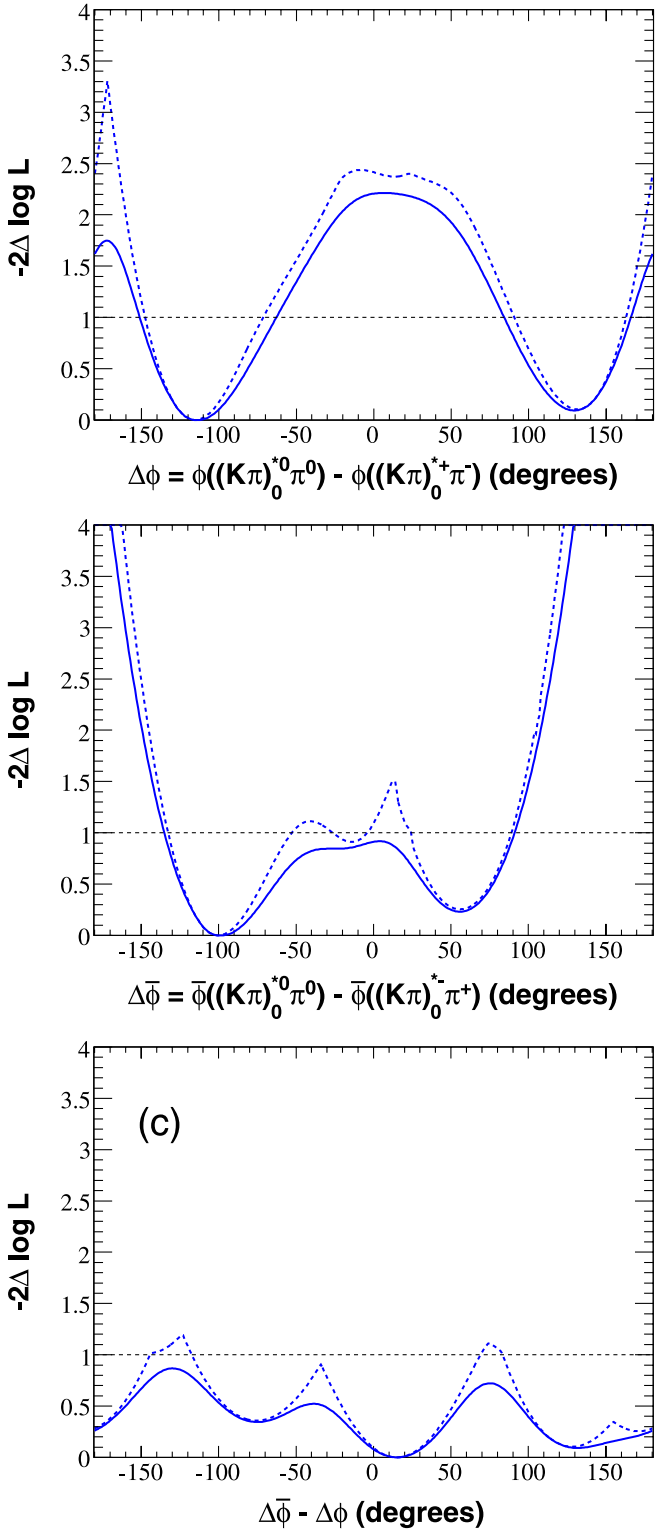

FIG. 11 (color online). The phase difference between the $(K\pi)_0^{*0}$ and the $(K\pi)_0^{*\pm}$ S-waves. The three diagrams are the NLL scans for the B^0 (a) and $\bar{B}^0$ decays (b) as well as their differences (c). The lines are drawn as in Fig. 10. The data do not indicate preferred angles. The four fit solutions find their NLL minimum for distinct phases.

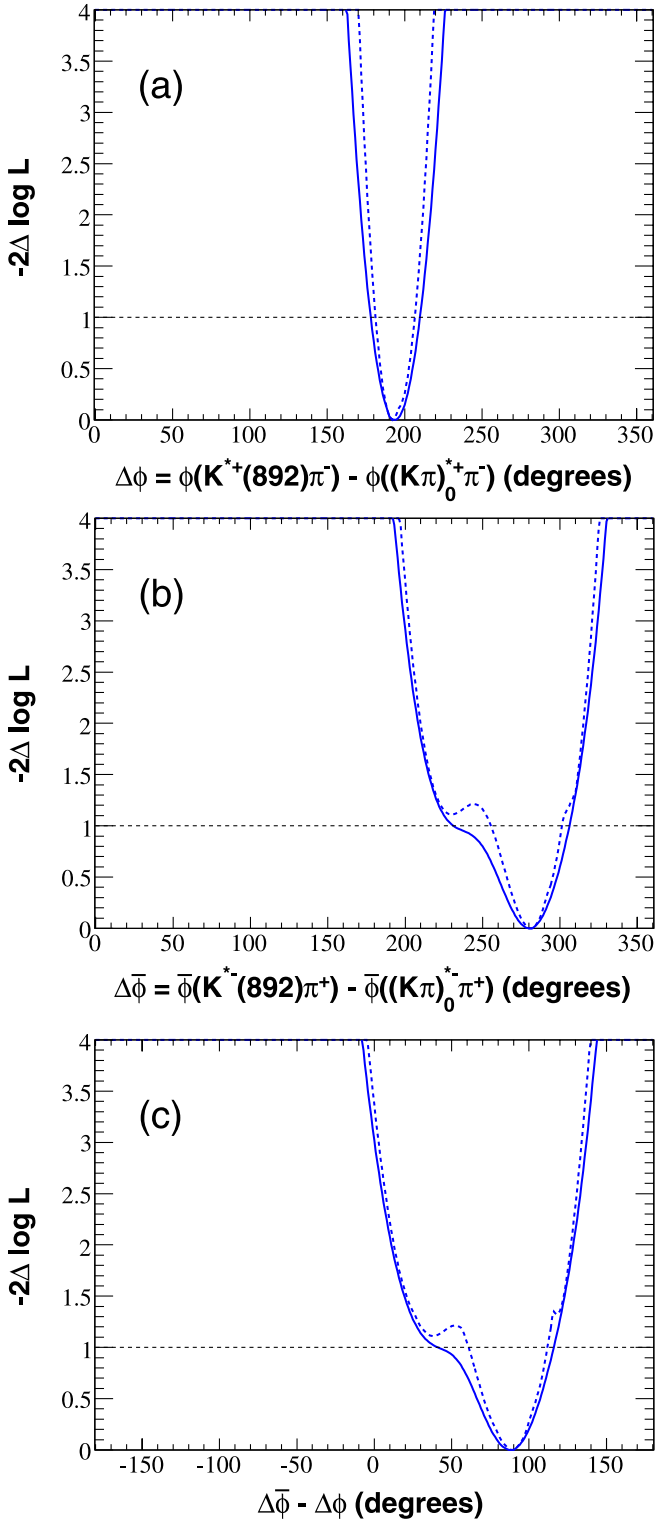

FIG. 12 (color online). The phase difference between the charged $K\pi$ P- and S-waves. The three diagrams are the NLL scans for the B^0 (a) and $\bar{B}^0$ (b) decays as well as their differences (c). The lines are drawn as in Fig. 10. The data provide significant constraints on these angles. The four fit solutions find their NLL minimum at approximately the same phase differences.

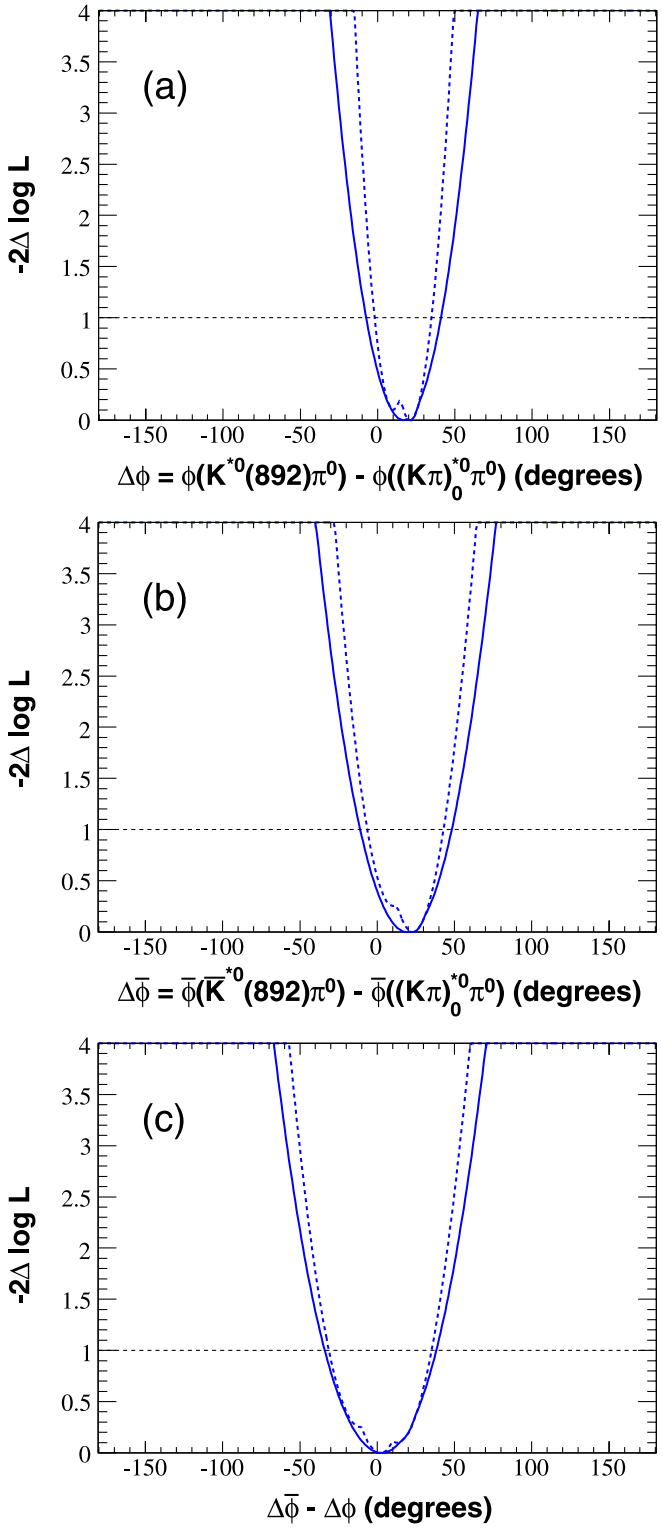

FIG. 13 (color online). The phase difference between the neutral $K\pi$ P- and S-waves. The three diagrams are the NLL scans for the B^0 (a) and $\bar{B}^0$ (b) decays as well as their differences (c). The lines are drawn as in Fig. 10. The data provide significant constraints on these angles. The four fit solutions find their NLL minimum at approximately the same phase differences.

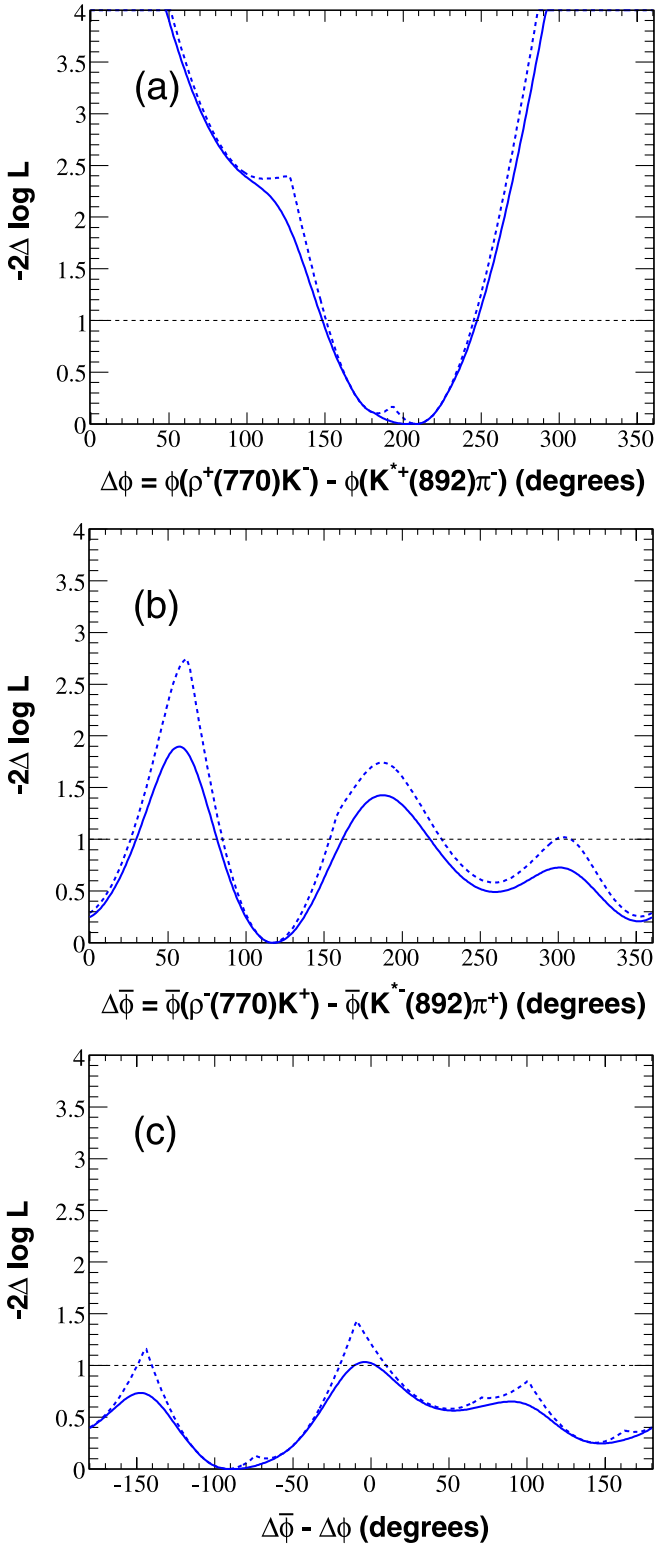

FIG. 14 (color online). The phase difference between the ρK and the charged $K\pi$ P-wave. The three diagrams are the NLL scans for the B^0 (a) and $\bar{B}^0$ (b) decays as well as their differences (c). The lines are drawn as in Fig. 10. The vertical scale cuts off $\Delta\chi^2 = 4$; however, it has been checked that all phase differences are consistent with the data at the 3 standard deviation level.

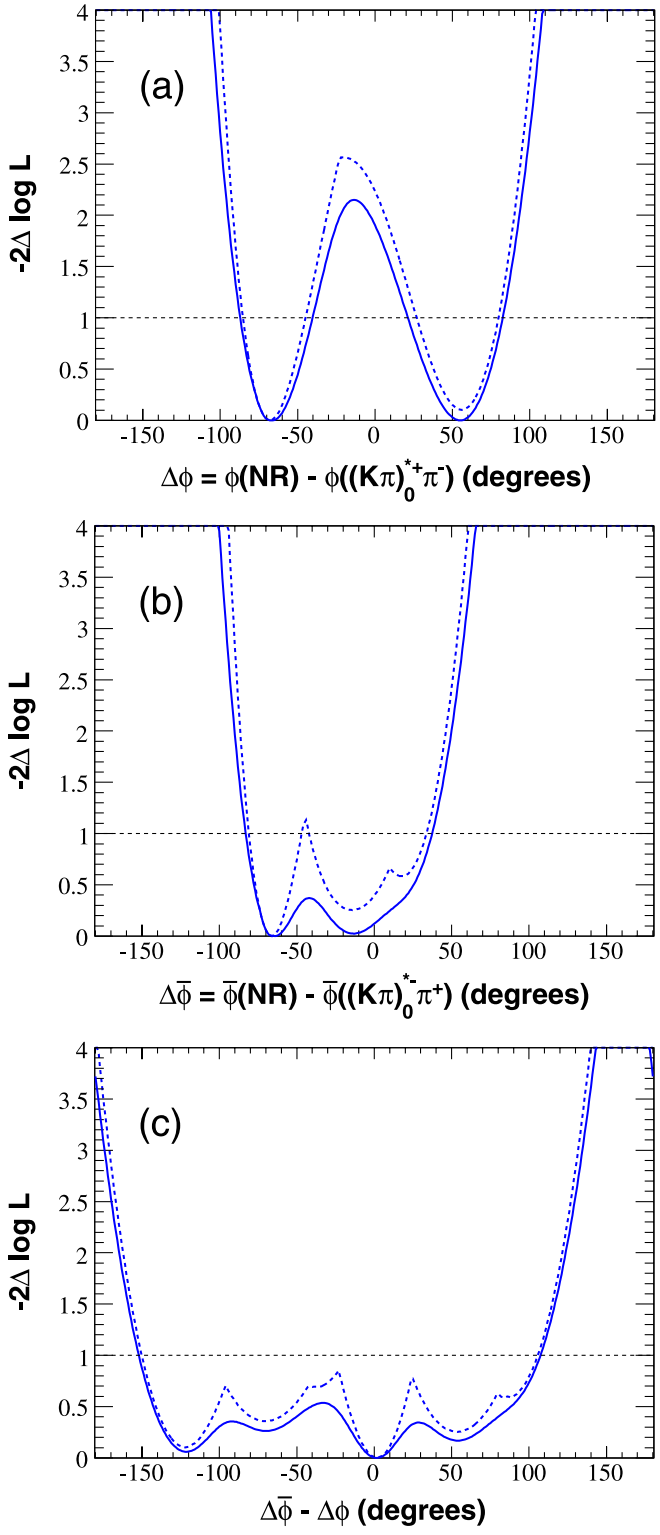

FIG. 15 (color online). The phase difference between the nonresonant $K^+\pi^-\pi^0$ and the charged $K\pi$ S-wave. The three diagrams are the NLL scans for the B^0 (a) and $\bar{B}^0$ (b) decays as well as their differences (c). The lines are drawn as in Fig. 10. Ranges with widths of 140 (a) and 190 (b) degrees are excluded at the 95% confidence level for the B^0 and $\bar{B}^0$ decays. No significant difference between the B^0 and $\bar{B}^0$ interference patterns is seen.

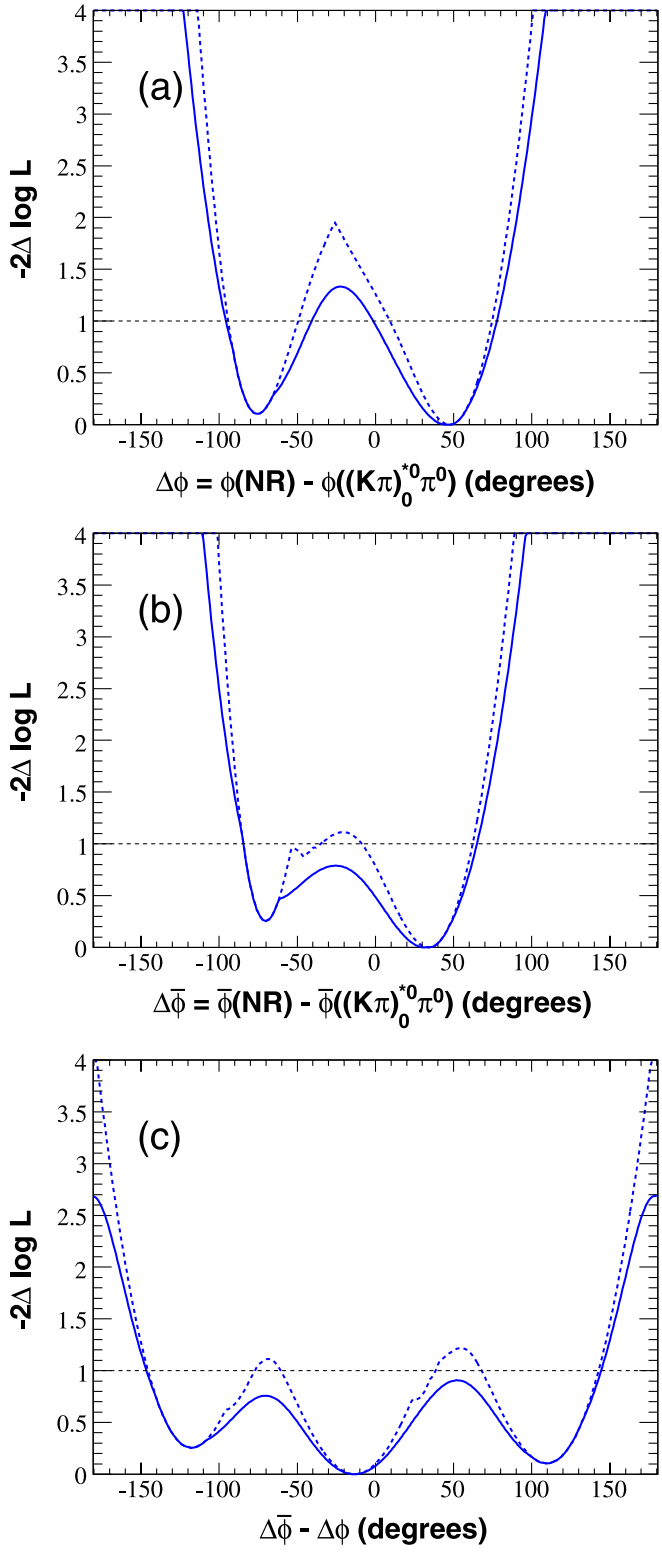

FIG. 16 (color online). The phase difference between the nonresonant $K^+\pi^-\pi^0$ and the neutral $K\pi$ S-wave. The three diagrams are the NLL scans for the B^0 (a) and $\bar{B}^0$ (b) decays as well as their differences (c). The lines are drawn as in Fig. 10. Ranges with widths of 90 (a) and 110 (b) degrees are excluded at the 95% confidence level for the B^0 and $\bar{B}^0$ decays. No significant difference between the B^0 and $\bar{B}^0$ interference patterns is seen.

resonances in B^0 decays, $\Delta\bar{\phi}_{ij} \equiv \bar{\phi}_j - \bar{\phi}_i$, the same for $\bar{B}^0$ decays, and $\delta\phi_{ij} \equiv \Delta\bar{\phi}_{ij} - \Delta\phi_{ij}$. A marked minimum in a $\Delta\phi$ ($\Delta\bar{\phi}$) scan indicates a sizable interference in B^0 ($\bar{B}^0$) decays. Evidence for direct CP violation would be seen if $\delta\phi_{\rm min} \equiv \Delta\bar{\phi}_{\rm min} - \Delta\phi_{\rm min}$ were significantly away from zero. The bounds which define the 1 standard deviation confidence intervals (1σ c.i.) are graphically seen as the intersection points between the solid scan curves (which incorporate both statistical and systematic uncertainties) and the $\Delta\chi^2 = 1$ horizontal line. The results are collected in Table VII. All isobar pairs for which the 95% confidence intervals in $\delta\phi$ are nontrivial (smaller than ± 180 degrees) exhibit sizable interference patterns in B^0 and $\bar{B}^0$ decays. The $\Delta\chi^2$ value for $\delta\phi = 0$ corresponds to the square of the direct CP-violation significance in standard deviation units. A scan of the R_i and R_j line shapes with more statistics could enable one to disentangle the strong phase motions and determine the weak phase. For the scans where interference is elusive, we quote in Table VII the maximum $\Delta\chi^2$ over the ± 180 degrees scanned range. For the $K\pi$ systems, we see no significant interference pattern between charged and neutral P-waves (Fig. 10) at the 95% confidence level, and similarly for the S-waves (Fig. 11). Only a small range ($\Delta\bar{\phi}$ between -131 and -75 degrees) is excluded at the 2 standard deviation level for the $\bar{B}^0$ P-waves. These observations are not unexpected for the $K^*(892)\pi$ final states since the K^* resonances are quite narrow and therefore have a small overlap in the Dalitz plot. Furthermore, the coherent sum of amplitudes that interfere might behave like the model in [5,6] with a single weak phase (equal to $\gamma_{\rm CKM}$ in the absence of electroweak penguin diagrams). In such a scheme, one weak phase would be missing to enable direct CP violation to take place. In contrast, Figs. 12 and 13 show that we measure, with uncertainties smaller than ± 36 degrees, the phase differences between the $K\pi$ S- and P-waves of the same charge for the B^0 and $\bar{B}^0$ decays. Moreover, the associated CP observables $\delta\phi$ are measured to 35 degrees with negligible systematic uncertainties (less than 10 degrees). An interval of order 220 degrees is excluded at the 95% confidence level. The charged and neutral S- and P-wave interference patterns thus provide sensitivity to two weak phases.

The scans of the phase differences between ρK and $K^*(892)\pi$ show no evidence for interference at the 3 standard deviation level, as shown in Fig. 14. Here again the overlap in phase space between the interfering resonances is small. This contrasts with what we observe in the scans of the phase differences between the nonresonant $K^\pm\pi^\mp\pi^0$ and the S-waves in Figs. 15 and 16. We see that they are somewhat constrained. These observations are in agreement with the fact that the fit finds a sizable nonresonant $B^0 \to K^+\pi^-\pi^0$ component that populates the Dalitz plot far from the boundary.

IX. SUMMARY

We have measured the branching fraction and CP asymmetry of the $B^\pm \to K^\pm\pi^\mp\pi^0$ decay and compared the Dalitz plots of $B^0 \to K^+\pi^-\pi^0$ and $\bar{B}^0 \to K^-\pi^+\pi^0$ using an isobar model. We have extracted the CP-averaged isobar branching fractions and CP asymmetries assuming no interference. We observe the $B^0 \to K^{*0}(892)\pi^0$ with 5.6 standard deviation significance. We have looked at the interference patterns in the Dalitz plots and put significant constraints on phase differences between wide intermediate states which have a sizable overlap in phase space. The phase shifts between S- and P-waves in the charged and neutral $K\pi$ and $\bar{K}\pi$ are constrained to within ± 70 degrees or less at the 95% confidence level. Weaker constraints are observed for the phase shifts between the $K(\bar{K})\pi$ and nonresonant components which extend widely over the Dalitz plots. The phase shift differences between $K\pi$ and $\bar{K}\pi$ S- and P-waves are measured and found to be consistent with no direct CP violation within 2 standard deviations. Additionally, we determine the branching fraction for the decay $B^0 \to \bar{D}^0\pi^0$ with an accuracy comparable to that of the world average value of this quantity.

ACKNOWLEDGMENTS

We are grateful for the extraordinary contributions of our PEP-II colleagues in achieving the excellent luminosity and machine conditions that have made this work possible. The success of this project also relies critically on the expertise and dedication of the computing organizations that support *BABAR*. The collaborating institutions wish to thank SLAC for its support and the kind hospitality extended to them. This work is supported by the U.S. Department of Energy and National Science Foundation, the Natural Sciences and Engineering Research Council (Canada), the Commissariat à l'Energie Atomique and Institut National de Physique Nucléaire et de Physique des Particules (France), the Bundesministerium für Bildung und Forschung and Deutsche Forschungsgemeinschaft (Germany), the Istituto Nazionale di Fisica Nucleare (Italy), the Foundation for Fundamental Research on Matter (The Netherlands), the Research Council of Norway, the Ministry of Education and Science of the Russian Federation, Ministerio de Educación y Ciencia (Spain), and the Science and Technology Facilities Council (United Kingdom). Individuals have received support from the Marie-Curie IEF program (European Union) and the A. P. Sloan Foundation.

APPENDIX

The four solutions of the fit are displayed in Table IX. The correlation coefficients of solution I are given in Tables X and XI. As explained in Sec. VI the statistical uncertainty of each solution does not reflect the actual experimental uncertainty and should not be used. The

TABLE IX. Results of the four solutions of the fit. The fractions are the CP-averaged isobar fractions (FF_j) defined with the CP asymmetries A_{CP} in Sec. II [Eq. (14)]. The phases ϕ for the B^0 decays and $\bar{\phi}$ for the $\bar{B}^0$ decays are measured relative to $B^0(\bar{B}^0) \to K^{*\pm}\pi^{\mp}$. The uncertainties are statistical only. They are underestimated because a parabolic approximation is made for the shape of the NLL close to the minimum.

		I	II	III	IV
$\mathrm{NLL_{min}}$		$-91\,079.6$	$-91\,079.5$	$-91\,079.4$	$-91\,079.5$
$K^{*+}(892)\pi^-$	Fraction (%)	$11.75^{+1.80}_{-1.47}$	$11.81^{+1.80}_{-1.44}$	$12.34^{+1.87}_{-1.46}$	$12.48^{+1.78}_{-1.52}$
	A_{CP}	$-0.19^{+0.13}_{-0.14}$	$-0.20^{+0.13}_{-0.14}$	$-0.12^{+0.13}_{-0.14}$	$-0.14^{+0.13}_{-0.14}$
	ϕ (deg.)	0 (fixed)	0 (fixed)	0 (fixed)	0 (fixed)
	$\bar{\phi}$ (deg.)	0 (fixed)	0 (fixed)	0 (fixed)	0 (fixed)
$K^{*0}(892)\pi^0$	Fraction (%)	$6.72^{+1.29}_{-1.26}$	$6.57^{+1.35}_{-1.19}$	$6.52^{+1.36}_{-1.21}$	$6.47^{+1.29}_{-1.27}$
	A_{CP}	-0.09 ± 0.19	-0.08 ± 0.19	$-0.12^{+0.19}_{-0.21}$	$-0.12^{+0.21}_{-0.19}$
	ϕ (deg.)	73.4 ± 37.1	306.6 ± 37.8	73.8 ± 37.4	305.8 ± 37.9
	$\bar{\phi}$ (deg.)	1.5 ± 38.8	1.0 ± 38.7	139.3 ± 45.4	140.5 ± 45.4
$(K\pi)^{*+}_0\pi^-$	Fraction (%)	$31.20^{+3.14}_{-2.91}$	$24.77^{+2.83}_{-2.86}$	$28.40^{+4.36}_{-3.97}$	$21.41^{+4.43}_{-3.75}$
	A_{CP}	$+0.07^{+0.11}_{-0.09}$	$+0.37 \pm 0.11$	$-0.03^{+0.15}_{-0.16}$	$+0.27^{+0.15}_{-0.18}$
	ϕ (deg.)	167.8 ± 10.8	164.7 ± 11.8	168.6 ± 10.8	165.4 ± 11.8
	$\bar{\phi}$ (deg.)	79.0 ± 19.1	78.8 ± 19.2	72.7 ± 16.6	72.5 ± 16.7
$(K\pi)^{*0}_0\pi^0$	Fraction (%)	$17.56^{+2.87}_{-2.62}$	$24.12^{+2.96}_{-2.81}$	$24.42^{+2.94}_{-2.77}$	$31.00^{+3.02}_{-2.83}$
	A_{CP}	$-0.31^{+0.17}_{-0.15}$	$-0.49^{+0.13}_{-0.12}$	$+0.05 \pm 0.12$	$-0.17^{+0.10}_{-0.11}$
	ϕ (deg.)	52.3 ± 36.9	296.3 ± 34.6	53.0 ± 37.2	295.8 ± 34.6
	$\bar{\phi}$ (deg.)	338.5 ± 38.9	337.9 ± 38.8	128.9 ± 37.5	130.0 ± 37.5
$\rho(770)^- K^+$	Fraction (%)	$22.60^{+2.07}_{-2.08}$	$21.77^{+2.07}_{-2.03}$	$21.64^{+2.10}_{-2.04}$	$20.88^{+2.08}_{-2.03}$
	A_{CP}	$+0.10 \pm 0.10$	$+0.14^{+0.10}_{-0.11}$	$+0.06^{+0.10}_{-0.11}$	$+0.10 \pm 0.11$
	ϕ (deg.)	208.5 ± 35.8	183.8 ± 33.5	206.8 ± 36.7	181.4 ± 33.7
	$\bar{\phi}$ (deg.)	117 ± 33.7	115.9 ± 33.6	351.1 ± 40.5	351.4 ± 39.8
NR	Fraction (%)	$12.51^{+2.22}_{-2.17}$	$12.78^{+2.28}_{-2.12}$	$11.90^{+2.27}_{-2.05}$	$12.24^{+2.22}_{-2.09}$
	A_{CP}	$+0.23^{+0.18}_{-0.19}$	$+0.19^{+0.19}_{-0.17}$	$+0.18 \pm 0.19$	$+0.15^{+0.18}_{-0.19}$
	ϕ (deg.)	99.9 ± 22.9	220.8 ± 24.8	100.0 ± 22.8	220.5 ± 25.0
	$\bar{\phi}$ (deg.)	12.7 ± 23.7	12.0 ± 23.6	58.6 ± 34.9	59.8 ± 35.0
	Total fraction (%)	102.4 ± 3.6	$101.8^{+3.6}_{-3.4}$	$105.3^{+4.6}_{-3.9}$	$104.5^{+4.5}_{-3.7}$

procedure we have devised blends all four solutions and determines reliable statistical and systematic uncertainties. For illustration, we display the four NLL around their minima in Fig. 17 for the isobar fractions and in Fig. 18 for the CP asymmetries. For the neutral S-wave final states, the spread due to the degeneracy of the fitted fractions and asymmetries is quite large.

TABLE X. Matrix of the correlation coefficients between the fitted parameters for the B^0 Dalitz plot in solution I.

Variable	$t_{(K\pi)^{*+}_0}$	$t_{(K\pi)^{*0}_0}$	$t_{K^{*0}(892)}$	t_{NR}	$t_{\rho(770)}$	$\phi_{(K\pi)^{*+}_0}$	$\phi_{(K\pi)^{*0}_0}$	$\phi_{K^{*0}(892)}$	ϕ_{NR}	$\phi_{\rho(770)}$
$t_{(K\pi)^{*+}_0}$	100.0									
$t_{(K\pi)^{*0}_0}$	-0.9	100.0								
$t_{K^{*0}(892)}$	7.3	-9.3	100.0							
t_{NR}	40.6	-27.4	1.9	100.0						
$t_{\rho(770)}$	17.3	11.9	8.6	3.9	100.0					
$\phi_{(K\pi)^{*+}_0}$	-9.1	0.8	0.2	7.0	1.3	100.0				
$\phi_{(K\pi)^{*0}_0}$	-31.7	53.0	-6.0	-15.0	-6.9	32.1	100.0			
$\phi_{K^{*0}(892)}$	-31.0	50.1	-5.5	-14.2	-4.9	31.5	93.2	100.0		
ϕ_{NR}	-47.2	12.9	3.8	-19.5	-6.6	54.2	61.0	61.1	100.0	
$\phi_{\rho(770)}$	-35.0	5.3	-7.5	-17.5	-20.4	31.9	44.1	37.4	52.4	100.0

TABLE XI. Matrix of the correlation coefficients between the fitted parameters for the $\bar{B}^0$ Dalitz plot in solution I.

Variable	$\bar{t}_{(K\pi)_0^{*-}}$	$\bar{t}_{(\bar{K}\pi)_0^{*0}}$	$\bar{t}_{K^{*-}(892)}$	$\bar{t}_{\bar{K}^{*0}(892)}$	$\bar{t}_{\mathrm{NR}}$	$\bar{t}_{\rho(770)}$	$\bar{\phi}_{(K\pi)_0^{*-}}$	$\bar{\phi}_{(\bar{K}\pi)_0^{*0}}$	$\bar{\phi}_{\bar{K}^{*0}(892)}$	$\bar{\phi}_{\mathrm{NR}}$	$\bar{\phi}_{\rho(770)}$
$\bar{t}_{(K\pi)_0^{*-}}$	100.0										
$\bar{t}_{(\bar{K}\pi)_0^{*0}}$	−1.4	100.0									
$\bar{t}_{K^{*-}(892)}$	9.1	0.7	100.0								
$\bar{t}_{\bar{K}^{*0}(892)}$	7.0	−18.9	6.4	100.0							
$\bar{t}_{\mathrm{NR}}$	33.3	−18.4	6.2	0.9	100.0						
$\bar{t}_{\rho(770)}$	20.4	1.7	9.7	8.2	6.8	100.0					
$\bar{\phi}_{(K\pi)_0^{*-}}$	5.2	−0.1	−9.7	−0.5	6.1	−3.3	100.0				
$\bar{\phi}_{(\bar{K}\pi)_0^{*0}}$	−27.7	59.1	−13.1	−10.2	−6.1	−13.9	42.2	100.0			
$\bar{\phi}_{\bar{K}^{*0}(892)}$	−25.6	52.9	−11.7	−6.0	−6.6	−12.2	40.9	86.9	100.0		
$\bar{\phi}_{\mathrm{NR}}$	−39.0	6.2	−16.2	−0.3	−7.5	−11.9	72.6	62.3	60.3	100.0	
$\bar{\phi}_{\rho(770)}$	−38.1	6.2	−18.0	−10.3	−4.1	−11.8	50.0	53.8	47.3	70.0	100.0

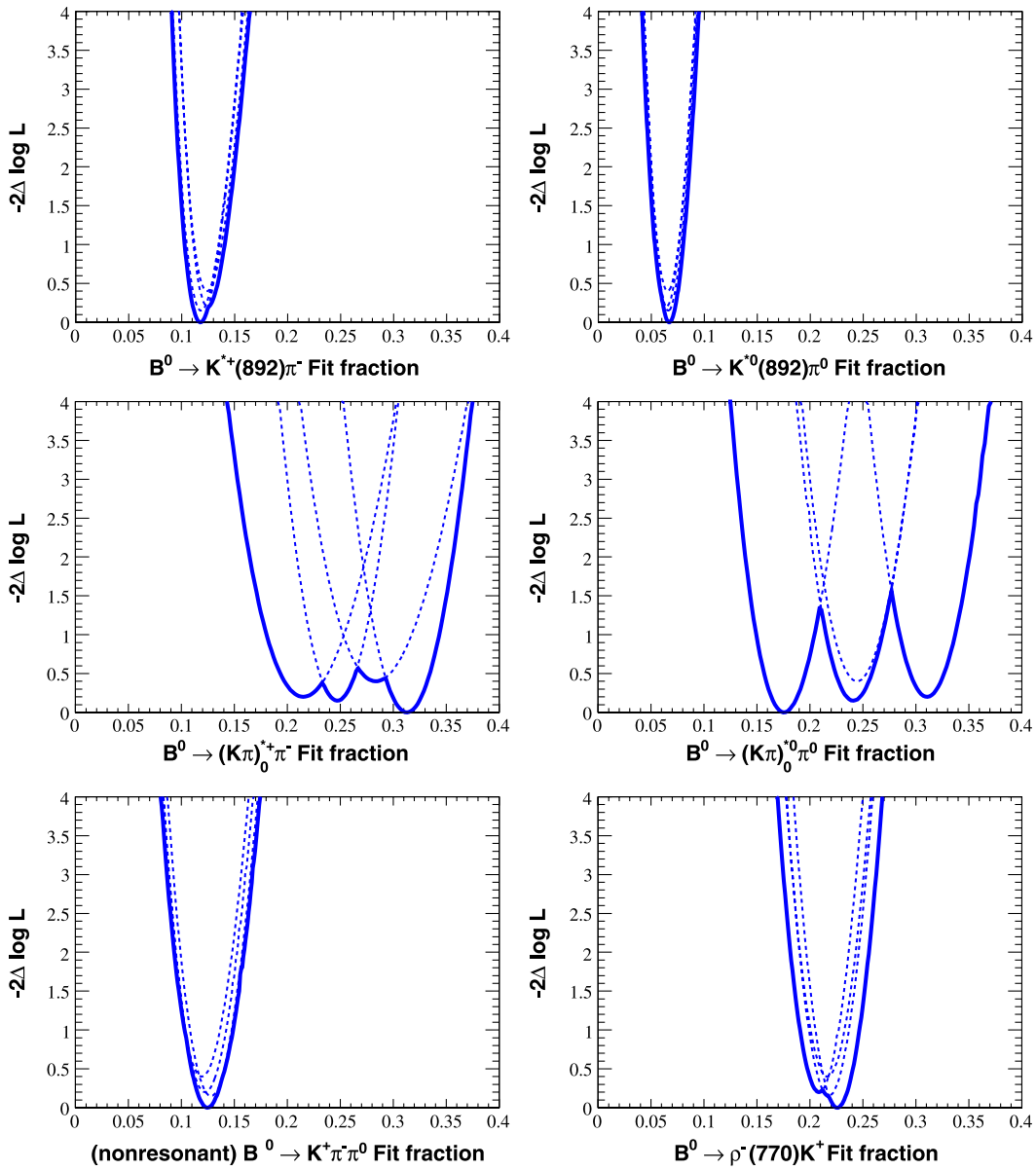

FIG. 17 (color online). The NLL functions for the isobar fractions. The NLL functions of each solution are shown with dashed lines. The fitted values for the $B \rightarrow (K\pi)_0^{*0}\pi$ in the four solutions are quite distinct. The envelope curves (solid lines) are used to quote the physical results.

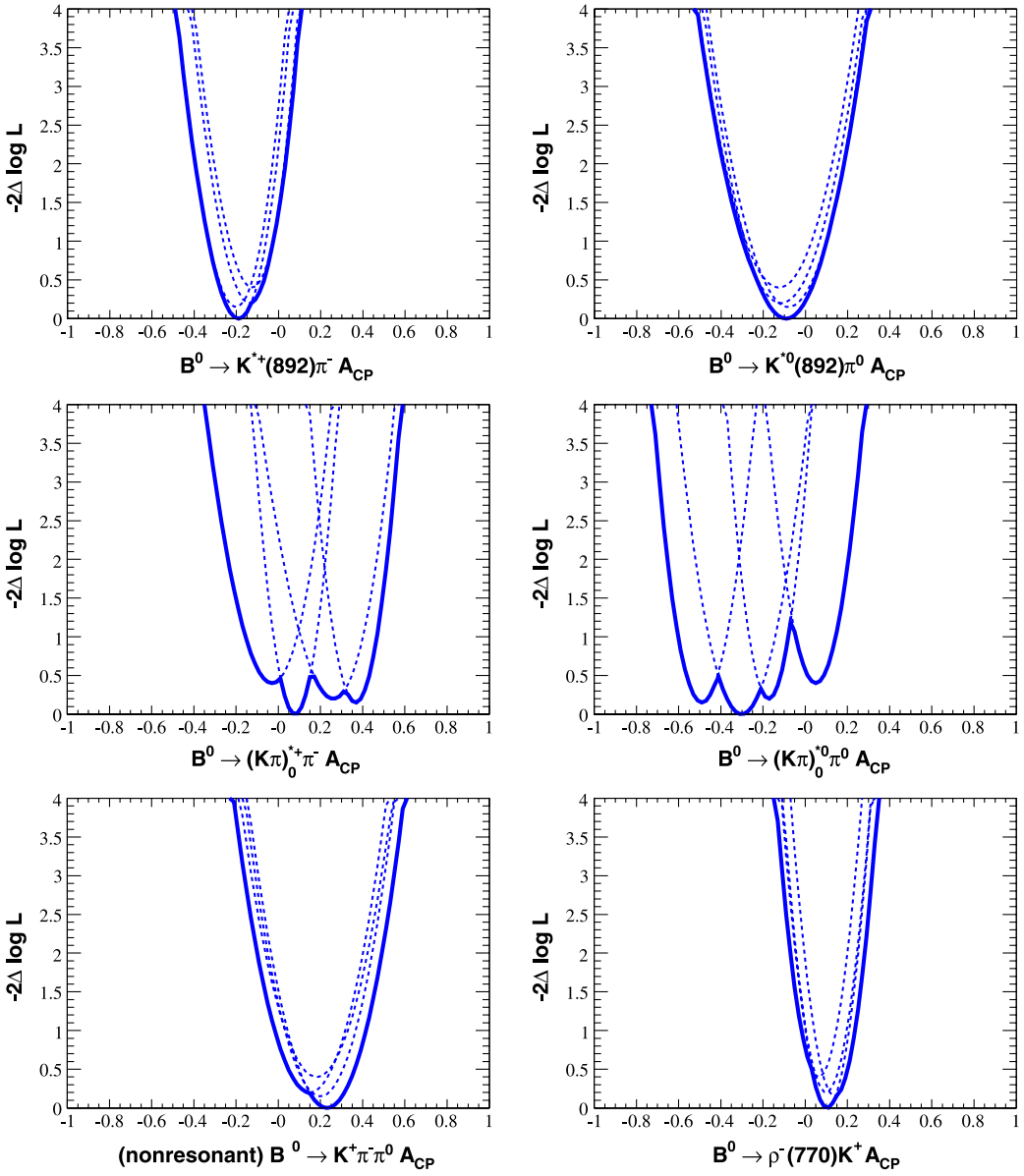

FIG. 18 (color online). The NLL functions for the *CP* asymmetries. The NLL functions of each solution are shown with dashed lines. The fitted values for the $B \to (K\pi)_0^{*0}\pi$ in the four solutions are quite distinct. The envelope curves (solid lines) are used to quote the physical results.

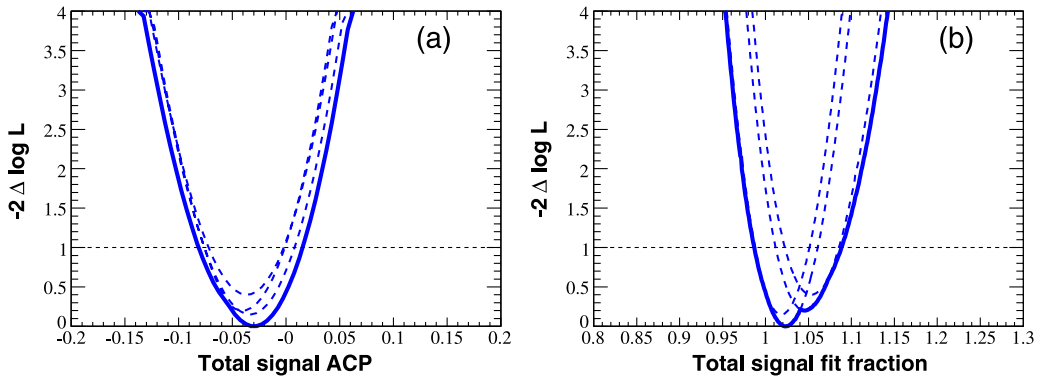

FIG. 19 (color online). NLL scans for the global *CP* asymmetry (a) and the total isobar fraction (b). The scans of each solution are shown with dashed lines. The envelope curves (solid lines) are the scans that are used to quote the physical results.

When the NLL are far from being parabolic at their minima, actual scans as described at the end of Sec. V are performed to derive the results. Figure 19 shows two examples of such scans for the sum of the isobar fit fractions (or the total fit fraction) and for the global *CP* asymmetry $\mathcal{A}_{CP}$ [Eq. (13)].

[1] N. Cabibbo, Phys. Rev. Lett. **10**, 531 (1963); M. Kobayashi and T. Maskawa, Prog. Theor. Phys. **49**, 652 (1973).
[2] H. R. Quinn and A. E. Snyder, Phys. Rev. D **48**, 2139 (1993).
[3] B. Aubert *et al.* (*BABAR* Collaboration), Phys. Rev. D **76**, 012004 (2007).
[4] A. Kusaka *et al.* (Belle Collaboration), Phys. Rev. Lett. **98**, 221602 (2007).
[5] M. Ciuchini, M. Pierini, and L. Silvestrini, Phys. Rev. D **74**, 051301 (2006).
[6] M. Gronau, D. Pirjol, A. Soni, and J. Zupan, Phys. Rev. D **75**, 014002 (2007).
[7] Throughout the paper, whenever a mode is given, the charge conjugate is also implied.
[8] B. Aubert *et al.* (*BABAR* Collaboration), arXiv:hep-ex/0408073.
[9] Zhitang Yu, Ph.D. thesis [Report No. SLAC-R-815 (unpublished)].
[10] E. Eckhart *et al.* (CLEO Collaboration), Phys. Rev. Lett. **89**, 251801 (2002).
[11] P. Chang *et al.* (Belle Collaboration), Phys. Lett. B **599**, 148 (2004).
[12] C. P. Jessop *et al.* (CLEO Collaboration), Phys. Rev. Lett. **85**, 2881 (2000).
[13] B. Aubert *et al.* (*BABAR* Collaboration), Phys. Rev. D **76**, 011103 (2007).
[14] B. Aubert *et al.* (*BABAR* Collaboration), Phys. Rev. D **72**, 072003 (2005); **74**, 099903(E) (2006).
[15] A Garmash *et al.* (Belle Collaboration), Phys. Rev. Lett. **96**, 251803 (2006).
[16] B. Aubert *et al.* (*BABAR* Collaboration), Phys. Rev. D **73**, 031101 (2006).
[17] A Garmash *et al.* (Belle Collaboration), Phys. Rev. D **75**, 012006 (2007).
[18] H. Y. Cheng, C. K. Chua, and A. Soni, Phys. Rev. D **76**, 094006 (2007).
[19] J. Blatt and V. Weisskopf, *Theoretical Nuclear Physics* (John Wiley & Sons, New York, 1956).
[20] D. Asner, arXiv:hep-ex/0410014.
[21] C. Zemach, Phys. Rev. **133**, B1201 (1964).
[22] S. Eidelman *et al.* (Particle Data Group), Phys. Lett. B **592**, 1 (2004).
[23] D. Aston *et al.*, Nucl. Phys. **B296**, 493 (1988).
[24] W.-M. Yao *et al.* (Particle Data Group), J. Phys. G **33**, 1 (2006).
[25] G. J. Gounaris and J. J. Sakurai, Phys. Rev. Lett. **21**, 244 (1968).
[26] P. Estabrooks, Phys. Rev. D **19**, 2678 (1979).
[27] W. M. Dunwoodie (private communication).
[28] B. Aubert *et al.* (*BABAR* Collaboration), Nucl. Instrum. Methods Phys. Res., Sect. A **479**, 1 (2002).
[29] S. Agostinelli *et al.* (GEANT4 Collaboration), Nucl. Instrum. Methods Phys. Res., Sect. A **506**, 250 (2003).
[30] P. Gay, B. Michel, J. Proriol, and O. Deschamps, Pisa 1995, New computing techniques in physics research, 725 (1995).
[31] K. S. Cranmer, Comput. Phys. Commun. **136**, 198 (2001).
[32] J. E. Gaiser *et al.*, Phys. Rev. D **34**, 711 (1986).
[33] H. Albrecht *et al.* (ARGUS Collaboration), Z. Phys. C **48**, 543 (1990).
[34] B. Aubert *et al.* (*BABAR* Collaboration), Phys. Rev. Lett. **91**, 201802 (2003).
[35] E. Barberio *et al.* (Heavy Flavor Averaging Group (HFAG)), arXiv:0704.3575v1.